Ore Geology Reviews 65 (2015) 900–916

Contents lists available at ScienceDirect

Ore Geology Reviews

journal homepage: www.elsevier.com/locate/oregeorev

In-situ LA-ICP-MS trace elemental analyses of magnetite and Re–Os dating of pyrite: The Tianhu hydrothermally remobilized sedimentary Fe deposit, NW China

Xiao-Wen Huang [a], Jian-Feng Gao [b,*], Liang Qi [a], Mei-Fu Zhou [c]

[a] State Key Laboratory of Ore Deposit Geochemistry, Institute of Geochemistry, Chinese Academy of Sciences, Guiyang 550002, China
[b] State Key Laboratory for Mineral Deposits Research, Nanjing University, Nanjing 210093, China
[c] Department of Earth Sciences, The University of Hong Kong, Hong Kong, China

ARTICLE INFO

Article history:
Received 19 February 2014
Received in revised form 15 July 2014
Accepted 28 July 2014
Available online 11 August 2014

Keywords:
Re–Os isotopes
Pyrite
LA-ICP-MS
Magnetite
Remobilization
Tianhu Fe deposit

ABSTRACT

The Tianhu Fe deposit (>104 Mt at 42% TFe) in the Eastern Tianshan (NW China) is hosted in the schist, quartzite, marble, and amphibolite of the Neoproterozoic Tianhu Group. The deposit consists of disseminated, banded and massive ores. Metallic minerals are dominantly magnetite and pyrite, with minor titanite, pyrrhotite, chalcopyrite, and sphalerite. Gangue minerals include dolomite with minor forsterite, diopside, apatite, biotite, chlorite, tourmaline, tremolite, talc, calcite, and magnesite. Pyrite separates from ores have 10.7 to 54.7 ppb Re and 0.033 to 0.175 ppb common Os. Those from the massive ores have a model 1 isochron age of 535 ± 36 Ma (2σ), in agreement with the isochron age (528 ± 18 Ma) of pyrite from the banded ores by regression of seven Re–Os analyses. The Re–Os age of ~530 Ma reflects the timing of a hydrothermal event that remobilized the Tianhu deposit. Magnetite has Mg, Al, Ti, V, Mn, Zn, and Ga contents ranging from ~5 to 3500 ppm and Cr, Co, Ni, and Sn contents ranging from ~1 to 200 ppm. Most magnetite grains have Ca + Al + Mn and Ti + V contents similar to those of the banded iron formation (BIF). Some grains have elevated Ti and V contents, indicating that that magnetite was formed by sedimentary process and overprinted by hydrothermal activity. Pyrite has $\delta^{34}S_{CDT}$ values from −9.23 to 10.96‰, indicating that the sulfur was reduced from the marine sulfates either by bacterial or thermochemical processes. Pyrite has relatively high Co (~346 to 3274 ppm) but low Ni (~5.6 to 35.4 ppm) with Co/Ni ratios ranging from ~10 to 270, indicating remobilization from a volcanic–hydrothermal fluid. Therefore, the Tianhu Fe deposit was originally a sedimentary type deposit but was overprinted by a hydrothermal event related to volcanic activity.

1. Introduction

There are commonly magmatic, structure-related, sedimentary, and metamorphic iron deposits (Dill, 2010). Some deposits may have involved multiple hydrothermal events after the formation. These deposits are generally hosted in Precambrian metamorphic rocks and are characterized by banded structures/textures. Most Precambrian Fe deposits are deformed, metamorphosed, and dismembered, making precise dating difficult by using traditional lithophile isotopes. Moreover, the sources of ore-forming materials are not easy to constrain due to multiple tectonothermal events. It has been documented that Re–Os isotopic systematic of pyrite (sometimes Cu-sulfides) is robust for dating sedimentary mineralization system and can remain unaffected by greenschist-facies metamorphism (e.g. Huang et al., 2013b; Kirk et al., 2001; Selby et al., 2009). The initial $^{187}Os/^{188}Os$ ratios obtained from isochron diagrams can be used to infer the source of Os and by inference the other ore-forming metals (Mathur et al., 2000, 2002; Morgan et al., 2000). In addition to chronological studies, Re–Os isotopic systematic was also used to discuss the fluid mixing or fluid remobilization (e.g. Mathur et al., 2012; Spry et al., 2013). Therefore, Re–Os isotopes of pyrite may be suitable to date the pyrite-bearing Fe deposits and trace the mineralization process.

The Paleozoic Tianshan tectonic belt of the Central Asia Orogenic Belt has been recognized as an important polymetallic mineralization province in China (Wang et al., 2006) (Fig. 1). Numerous magmatic Fe deposits in the eastern part of the Tianshan tectonic belt are hosted in the gabbroic intrusions such as the Weiya deposit (Wang et al., 2005; Zhang et al., 2005) (Fig. 1b). There are also magmatic–hydrothermal Fe deposits hosted in volcanic rocks such as the Yamansu, Heifengshan,

* Corresponding author. Tel.: +86 13601450660.
E-mail address: gao_jianfeng@yahoo.com (J.-F. Gao).

http://dx.doi.org/10.1016/j.oregeorev.2014.07.020
0169-1368/

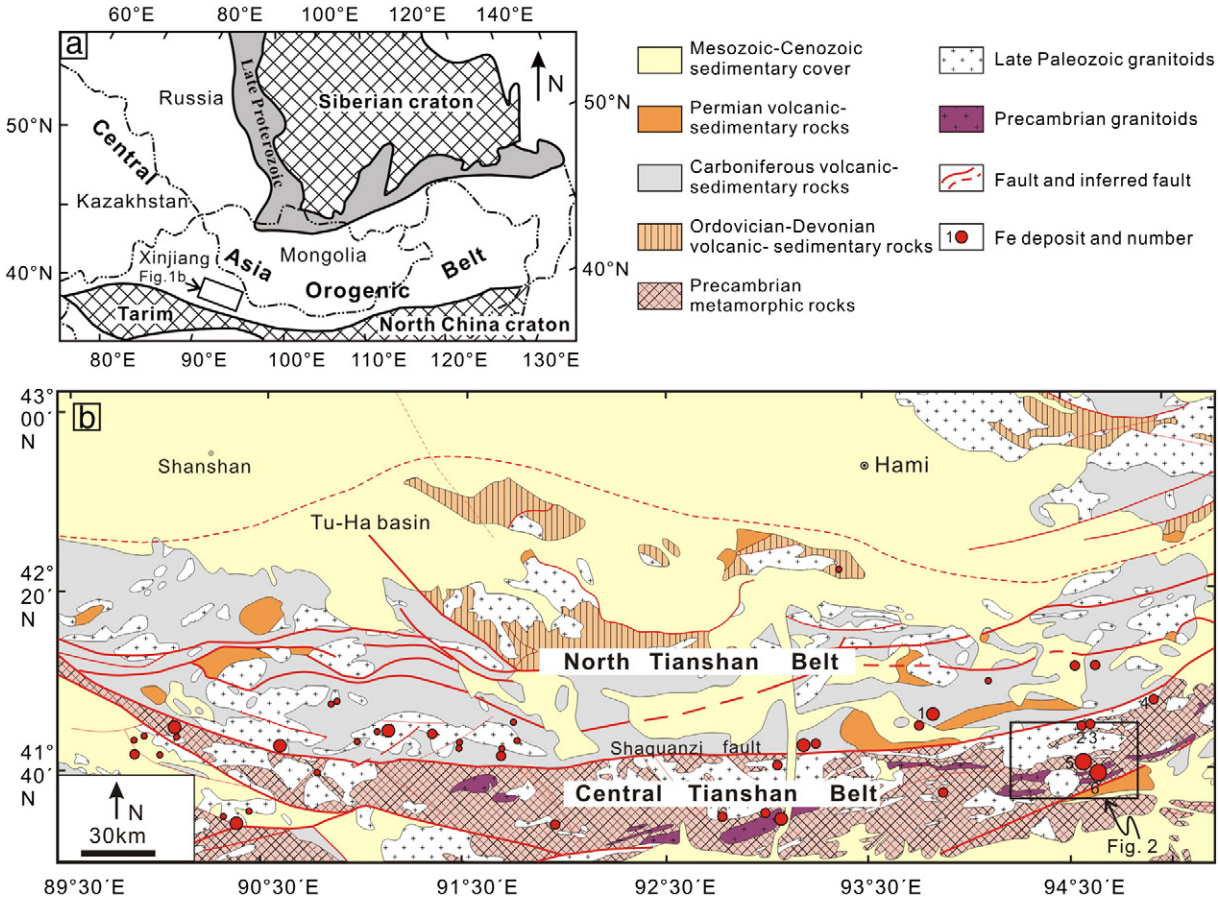

Fig. 1. (a) Location of the study area in the Central Asia Orogenic Belt (modified from Zhang et al., 2009). (b) Geological map of the Eastern Tianshan, also showing the distribution of Fe deposits (modified from 1:1,000,000 geological map of mineral resources of eastern Tianshan in 2008). Iron deposits: 1 — Yamansu deposit; 2 — Heifengshan deposit; 3 — Shuangfengshan deposit; 4 — Shaquanzi deposit; 5 — Weiya deposit; 6 — Tianhu deposit.

Shuangfengshan and Shaquanzi Fe(–Cu) deposits (Hou et al., 2014a,b; Huang et al., 2013a, 2014; Li and Chen, 2003; Mao et al., 2005; Zhang et al., 2014) (Fig. 1b). Being an exception, the Tianhu deposit is hosted in metamorphic rocks (Jia, 1991; Song et al., 1989). Being one of the largest Fe deposits in the Tianshan tectonic belt, the Tianhu deposit has been mined since the 1960s and accounts for about 20% ore reserve of Fe deposits in the Tianshan tectonic belt (Chen, 2006). In spite of significant economic values, there are only sparse studies and the genesis of the Tianhu deposit remains a matter of debate. The deposit was thought as a contact metasomatic deposit (magnesian skarn deposit) (BNGEXUAR, 1976; Luo and Zhu, 1986; Zhang, 1985; Zhao, 1989) or metamorphosed sedimentary deposit overprinted by younger hydrothermal event (Chen, 2007; Jia, 1991; Song et al., 1989). Recent studies have demonstrated that in situ trace element compositions of magnetite by laser ablation-inductively coupled plasma-mass spectrometry (LA-ICP-MS) can reflect different styles of mineralization or fluid evolution processes (Beaudoin and Dupuis, 2009; Carew, 2004; Dare et al., 2012; Dupuis and Beaudoin, 2011; Gao et al., 2013; Huang et al., 2013c; Müller et al., 2003; Nadoll et al., 2012, 2014; Rusk et al., 2009; Singoyi et al., 2006). The main ore mineral, magnetite, of the Tianhu deposit, thus provides an opportunity to examine the origin of the deposit. In the Tianhu deposit, there is abundant pyrite that is ideal to investigate if it is formed during the sedimentary or hydrothermal process.

In this paper, we describe the geology of the Tianhu Fe deposit and report the Re–Os isotope age of pyrite and LA-ICP-MS data of magnetite. Sulfur isotope and trace element composition of pyrite were also obtained to constrain the origin of ore-forming fluids.

2. Geological background

2.1. Regional geology

The Central Asian Orogenic Belt (CAOB) is the largest Phanerozoic orogen in the world and was formed by multiple subduction–accretion and collision processes from the Neoproterozoic to the Late Paleozoic (Jahn et al., 2000, 2004; Sengör and Burtman, 1993; Windley et al., 2007; Xiao et al., 2008, 2009b). The Tianshan tectonic belt along the southern margin of the CAOB extends west–east for about 1500 km (Fig. 1a). The Tianshan tectonic belt was formed by subduction, accretion and collision of various continental blocks between the Siberia and Tarim–North China Cratons (Fig. 1a). The final amalgamation of these blocks occurred in the Late Carboniferous (Ji et al., 1994; Ma et al., 1993, 1997; Qin et al., 2002; Xia et al., 2008; Yang et al., 1997) or Permian (Xiao et al., 2009a).

The Eastern Tianshan consists of the North, Central and South Tianshan Belts (Fig. 1b). The North Tianshan Belt consists of Carboniferous calc-alkaline volcanic and sedimentary rocks, intruded by Permian–Carboniferous mafic and intermediate–felsic plutons. The Carboniferous rocks may have formed by northward or southward subduction of the oceanic crust (Pirajno et al., 2008). The South Tianshan Belt contains fragments of oceanic crust in fault contacts with middle Silurian to

middle Carboniferous sandstone, shale, chert and limestone, which were possibly deposited on a passive margin of the northern Tarim block (Carroll et al., 1995).

The Central Tianshan Belt is separated from the North Tianshan Belt by the Shaquanzi fault (Fig. 1b). The Central Tianshan Belt has been regarded as a composite volcanic arc composed of Precambrian basement rocks of amphibolite facies, overlain by calc-alkaline basaltic andesite, volcanoclastics, minor I-type granite and granodiorite (Xiao et al., 2004). The Precambrian basement consists of gneiss, quartz schist, migmatite, and marble, which has U–Pb and Sm–Nd ages ranging from 1400 to 1800 Ma (Chen et al., 1999; Hu et al., 2000). There are Ordovician basalt, andesite, dacite, rhyolite, greywacke, and Silurian turbidite (Shu et al., 2002). Early Silurian and Early Carboniferous active margin sequences are widespread in this belt (Fang, 1994; Zhang, 1994; Zhou et al., 2001). Silurian terrestrial clastic rocks and limestones are in conformable contact with those of Devonian. Overlying Silurian rocks are Early Carboniferous volcanic rocks. Carboniferous fossils in the Precambrian basement rocks are imbricated with deformed volcanics, clastics, limestones, and ultramafic rocks and were considered as remnants of volcanic arc because of their calc-alkali geochemistry (Fang, 1994; Zhou et al., 2001). Granitic rocks in the Central Tianshan Belt were possibly formed in the Precambrian or Carboniferous (BGMRXUAR, 1993). The Central Tianshan Belt is thus considered a remnant of an Andean-type magmatic arc possibly with N-dipping subduction polarity underneath its southern margins in the Late Ordovician–Silurian to Devonian–Early Carboniferous (Hu et al., 2000; Xiao et al., 2004). Recent studies have showed that the Central Tianshan Belt might have been part of the Tarim Block (Lei et al., 2011; Ma et al., 2012) and records the assembly of the Tarim Block within the Columbia supercontinent (Ma et al., 2013).

2.2. Geology of the Tianhu area

In the Tianhu area, the eastern part of the Central Tianshan Belt (Fig. 1b), Proterozoic basement is overlain by Cambrian rocks, Pre-

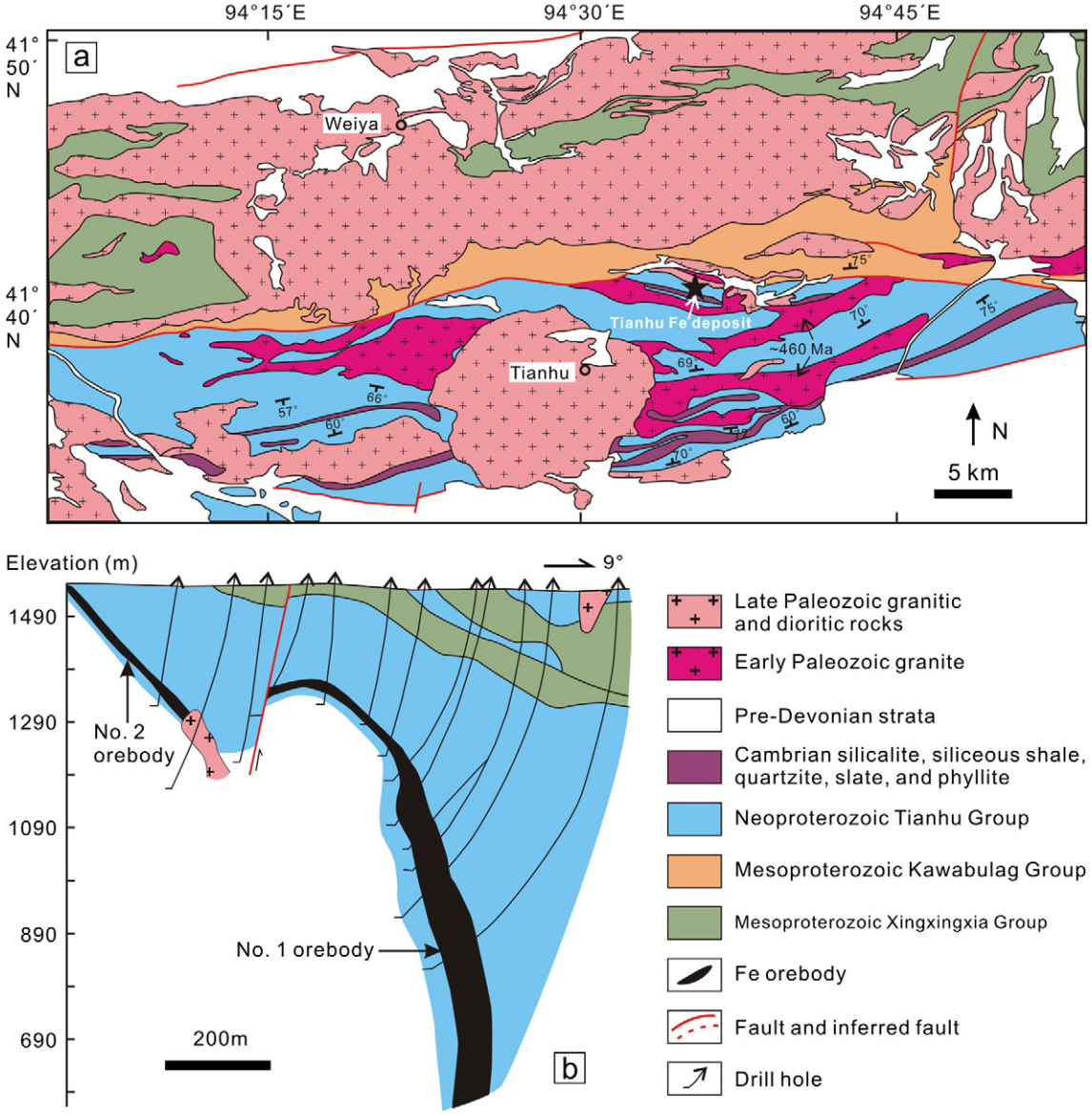

Fig. 2. (a) Geological map of Tianhu area showing the distribution of Paleozoic granitic and dioritic rocks (modified from 1:200,000 geological map of Shaquanzi area numbered K-46-23 in 1965). (b) Cross-section of No. 50 exploration line showing the occurrence of the larger No. 1 and No. 2 orebodies (modified from Yao et al., 1993).

Devonian strata, and Paleozoic granitic intrusions (Fig. 2a). The basement is represented by the Mesoproterozoic Xingxingxia and Kawabulag Groups and the Neoproterozoic Tianhu Group, and has been metamorphosed mainly to upper greenschist or amphibolite facies (Gao et al., 1993).

The Xingxingxia Group is mainly composed of granitic gneisses, marbles, migmatites, quartzites, and schists, which experienced greenschist and amphibolite facies and local to granulite facies metamorphism (Dong et al., 1996; Liu et al., 2004). The granitic gneisses and amphibolites in the Xingxingxia Group were thought to have prolithos of volcanic rocks or plutons (Hu et al., 1998). Sedimentary rocks of the Xingxingxia Group are considered to have deposited on an active continental margin or continental island-arc setting in the Late Mesoproterozoic and have sourced from Paleoproterozoic crust mixed with minor juvenile arc-magma materials at ~1.2 Ga (Li et al., 2005). The Xingxingxia Group was intruded by Early Paleozoic (~430 Ma) granodiorite (Lei et al., 2011).

The Kawabulag Group contains granitic gneisses, magnesium-enriched marbles, and minor terrestrial and tuffaceous clastic rocks (Liu et al., 2004). The Kawabulag Group is intruded by the ~1141 Ma granodiorite (Xiu et al., 2002).

The Tianhu Group comprises mainly schist, quartzite, marble, and minor amphibolite, which were metamorphosed from terrestrial clastic rocks and minor interbedded mafic volcanic rocks (Liu et al., 2004). It was probably formed between ~1000 and 660 Ma (Hu et al., 1986). The Tianhu Group was intruded by Early to Late Paleozoic granitic rocks, which have zircon U–Pb ages of ~460 Ma (Fig. 2a; Hu et al., 1986, 2007; Li et al., 2001).

3. Deposit geology

The Tianhu Fe deposit was discovered by a comprehensive survey in 1960 using geological and magnetic methods (Yao et al., 1993). The deposit contains >104 Mt (million tons) Fe ores with an average grade of 42% TFe and the ores with grade of 45% TFe exceed 30 Mt reserve (Chen, 2007). The deposit is hosted in the Tianhu Group with the most orebodies hosted in the dolomitic marble of the group. The mineralization zone is approximately 6 km long, 2 to 3 km wide, and covers an area of ~6 km^2. The ore-bearing sequence includes interbedded Fe ore layers and altered dolomitic marble in the upper and lower parts, and biotite–quartz schist in the middle part. Individual ore layers are commonly 2 to 10 m thick and ~1000 m deep with the largest thickness of 26.1 m. There are more than ten orebodies, among which the No. 1 orebody is the largest and accounts for 38.8% of the total ore reserve (Chen, 2007). Orebodies commonly appear in bedded, near-bedded and lenticular shapes. Generally, orebodies trend 97–100° with a north-dipping angle of 70–80°. Individual orebodies have a length of 50–120 m, thickness of 1–7 m and depth of 10–17 m. The No. 1 orebody has a length of 3760 m and a depth of 200 to 1000 m, and is composed of three ore layers (Yao et al., 1993) (Fig. 2b). Other orebodies are relatively small with a length of 50–750 m and depth of 0.3–2.7 m, and have ore grade ranging from 32 to 50% (Yao et al., 1993).

Hydrothermal alteration in the Tianhu Fe deposit formed tremolite, serpentinite, chlorite, actinolite, and talc. Dolomitic marble is commonly altered to talc–chlorite schist and serpentine. According to mineral assemblage and Fe content, ores can be divided into carbonate and silicate types. Carbonate type Fe ores commonly show disseminated and massive structures and have major gangue mineral of dolomite with minor chlorite, tremolite, calcite, and apatite. Silicate type Fe ores occur as disseminated and banded structures with gangue minerals dominated by tremolite, talc, serpentine, and olivine with minor dolomite, chlorite, muscovite, biotite, magnesite, apatite and calcite. Both types of ores contain pyrite, pyrrhotite, chalcopyrite, and sphalerite. Carbonate ores are commonly iron-rich with an average ore grade of 50.87%, whereas silicate ores are iron-poor with ore grades ranging from 32 to 38% (Chen, 2007; Song et al., 1989). Both types are commonly transitional in terms of mineral abundance.

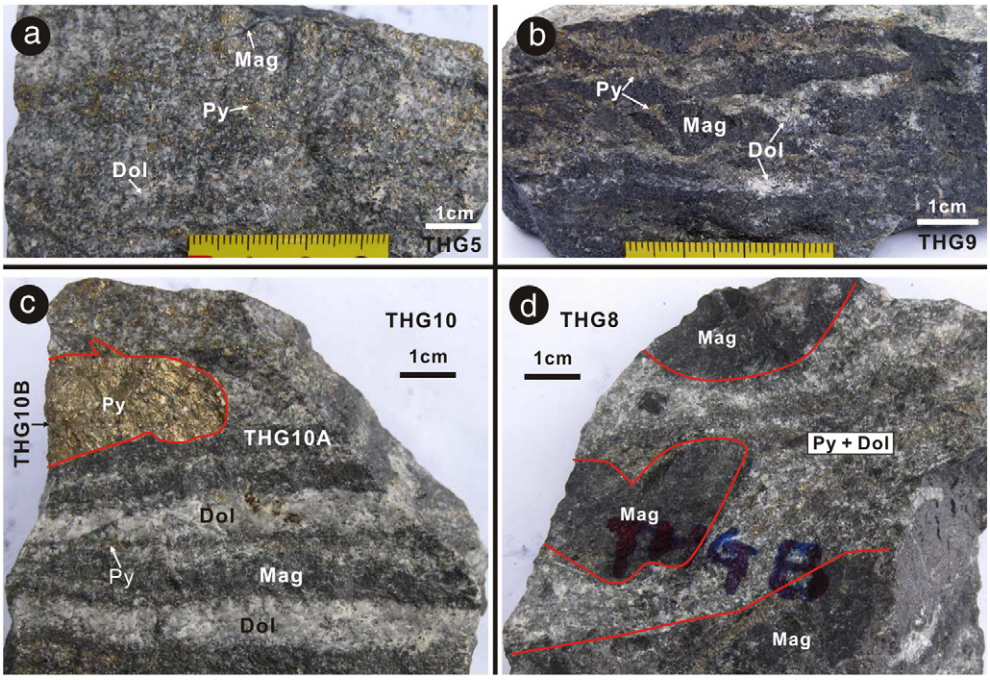

Fig. 3. Photos of ores from the Tianhu Fe deposit. (a) Disseminated ore composed of fine-grained magnetite, pyrite, and dolomite; (b) massive ore composed of magnetite, and minor pyrite and dolomite. The wave-like bands indicate that the ore may have suffered from intense deformation after its formation; (c) banded ore composed of interbedded magnetite, pyrite, and dolomite. The dark bands are composed of magnetite and pyrite, whereas the light bands consist of dolomite and pyrite. There are two types of pyrite, including fine-grained pyrite disseminated in the ore (THG10A) and coarse-grained pyrite injecting the ore (THG10B); (d) banded ore has a mineral assemblage of magnetite, pyrite, and dolomite. Pyrite–dolomite veins crosscut the ore, forming brecciated structure. Mag, magnetite; Py, pyrite; Dol, dolomite.

There are disseminated, massive, and banded ores (Fig. 3a–d). Different types of ores have similar mineral assemblage of magnetite, pyrite, and dolomite (Fig. 3). Some disseminated ores also contain biotite and chlorite associated with dolomite (Fig. 4a). Some pyrite grains in disseminated ores are well rounded (Fig. 4b). Pyrrhotite commonly infills the fracture of pyrite

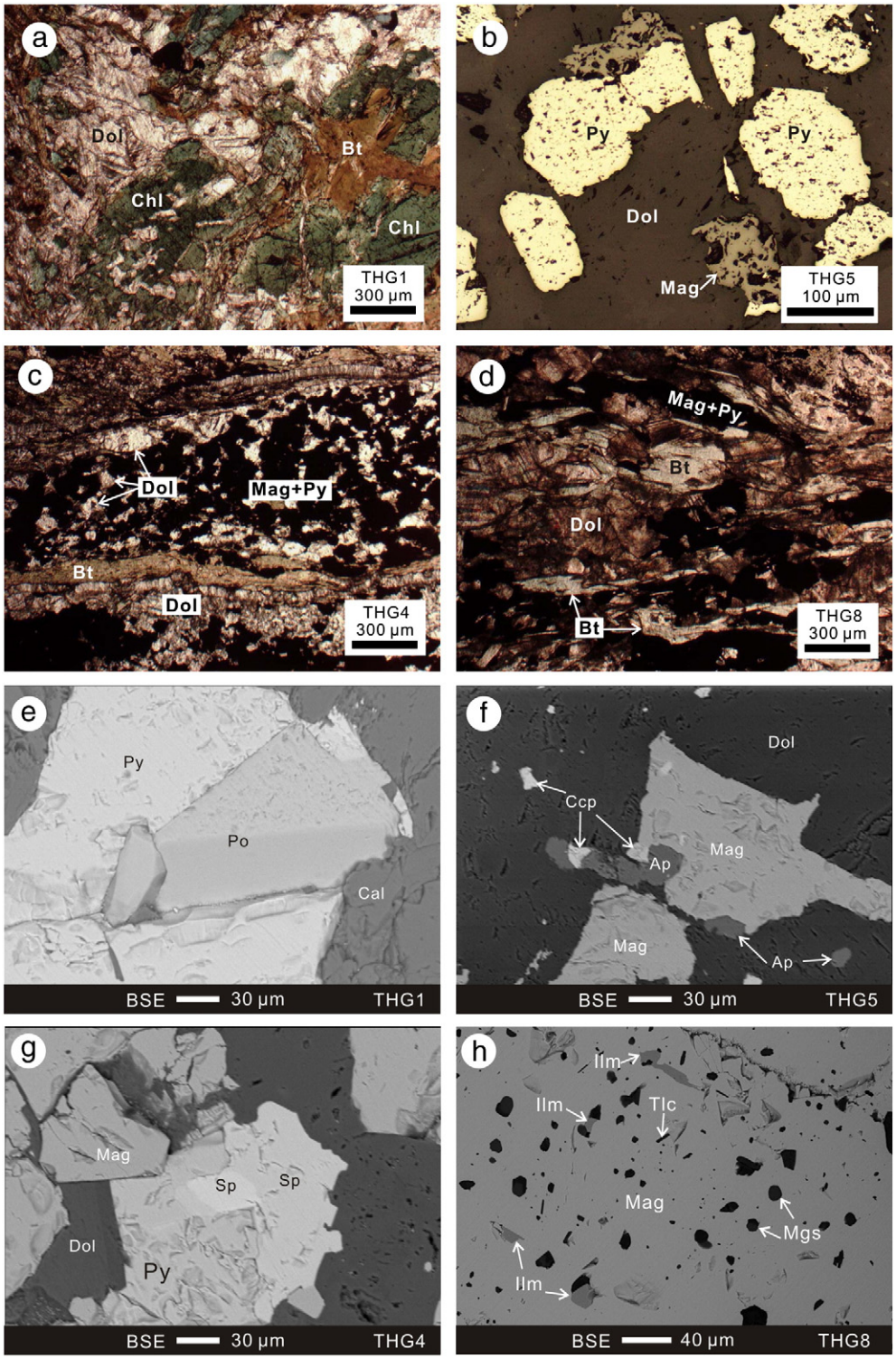

Fig. 4. Photomicrographs of ores from the Tianhu Fe deposit. (a) Disseminated ore contains gangue minerals of biotite, chlorite, and dolomite (under polarized light); (b) euhedral pyrite grains show good psephicity, indicating that pyrite has experienced transport process or suffered from metamorphism reformation after it formed (under reflected light); (c) bands of biotite, dolomite, and magnetite–pyrite parallel to each other (under polarized light). Some anhedral to subhedral dolomite grains infill the space between magnetite and pyrite; (d) bands of magnetite and pyrite parallel to biotite grains (under polarized light). Biotite was deformed due to modification process; (e) pyrrhotite infills pyrite grains, indicating the earlier formation of pyrite (BSE); (f) Chalcopyrite associated with magnetite, apatite and dolomite (BSE); (g) pyrite replaced by sphalerite and associated with magnetite, and dolomite (BSE). The differences in color of sphalerite may be due to the different contents of iron; (h) gangue minerals of ilmenite, magnesite, and talc enclosed in magnetite indicates their earlier formation (BSE). Ap, apatite; Bt, biotite; Ccp, chalcopyrite; Chl, chlorite; Dol, dolomite; Ilm, ilmenite; Mag, magnetite; Mgs, magnesite; Py, pyrite; Sp, sphalerite; Tlc, talc.

(Fig. 4e), and chalcopyrite usually replaces pyrite (Fig. 4f). Massive ores consist of ~90 modal% magnetite, ~5 modal% pyrite, and ~5 modal% dolomite, which retain relict bands (Figs. 3b and 4c). Pyrite is locally replaced by sphalerite (Fig. 4g). Banded ores are characterized by interbedded dark and light bands that are commonly one centimeter wide (Fig. 3c). The dark bands are composed of magnetite and pyrite, whereas light bands consist of dolomite ± biotite (Fig. 4d). Some banded ores show brecciated structures with later pyrite and dolomite veins infill the fracture of magnetite (Fig. 3d). Small ilmenite, magnesite, and talc grains are enclosed by magnetite, indicating their earlier formation (Fig. 4h).

The paragenesis of the Tianhu Fe deposit was controversial due to the complexity of minerals and multiple generations of some minerals. According to previous studies and our observation, four main stages of mineralization and alteration are recognized (Fig. 5) (BNGEXUAR, 1976). Stage 1 is dominantly sedimentary diagenesis, forming the dolomitic carbonate rocks. Stage 2 is the high-temperature hydrothermal stage (500–300 °C), which has a mineral assemblage of titanite, forsterite, diopside, enstatite, and minor apatite and tourmaline. Stage 3 is the middle-temperature (300–200 °C) hydrothermal stage, producing minerals that include magnetite, epidote, biotite, humite, hornblende, zoisite, tremolite, actinolite, and phlogopite. Stage 4 is low-temperature (<200 °C) mineralization stage, characterized by dolomite, quartz, chlorite, serpentine, fluorite, anhydrite, magnetite and large amounts of sulfides such as pyrite, pyrrhotite, chalcopyrite, and sphalerite. There are amounts of magnetite in stages 3 and 4.

4. Analytical results

Pyrite separates from the ores of the Tianhu Fe deposit were analyzed for Re–Os isotopes, sulfur isotopes, and trace elements. In situ

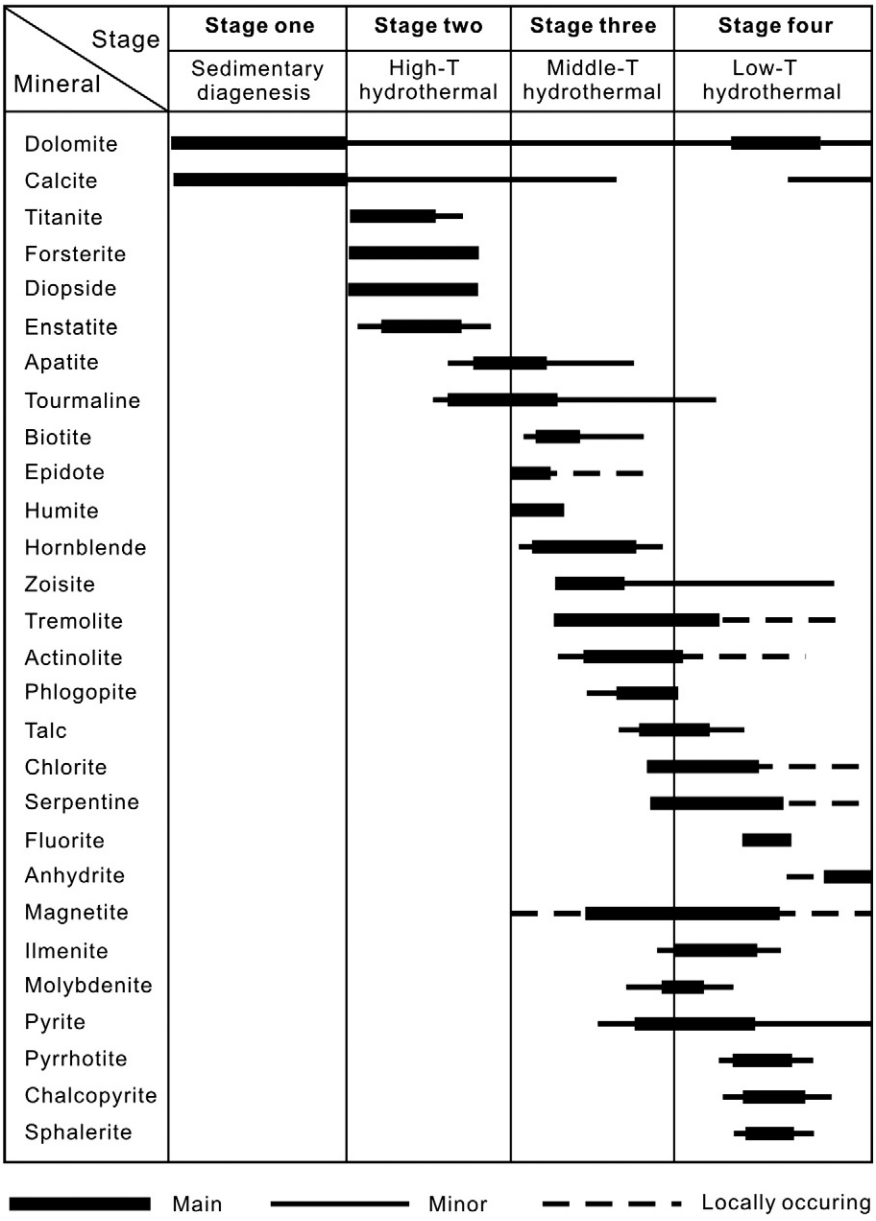

Fig. 5. Paragenetic sequence of alteration and mineralization at the Tianhu Fe deposit. Modified from BNGEXUAR (1976).

Table 1
Re–Os isotopic composition of pyrite from the Tianhu Fe deposit, NW China.

Sample no.[a]	Ore type	Weight (g)	Total Re (ppb)[b]	2σ	Total Os (ppb)[b]	2σ	Common Os (ppb)[b]	2σ	^{187}Re (ppb)[b]	2σ	^{187}Os (ppb)[b]	2σ	^{187}Re/^{188}Os[b]	2σ	^{187}Os/^{188}Os[b]	2σ	rho[c]	$(^{187}Os/^{188}Os)_i$[d]
THG1	Disseminated	0.1331	54.7	2.6	0.364	0.010	0.066	0.010	34.4	1.6	0.297	0.005	3963	637	33.7	5.2	0.95	−1.45
THG2	Disseminated	0.5036	31.8	0.8	0.174	0.003	0.036	0.002	20.0	0.5	0.138	0.003	4191	226	28.4	1.5	0.80	−8.77
THG2-DUP	Disseminated	0.5073	30.1	0.6	0.171	0.007	0.034	0.005	18.9	0.4	0.136	0.003	4216	678	29.9	4.8	0.98	−7.49
THG5	Disseminated	0.5057	20.0	1.3	0.135	0.003	0.034	0.003	12.6	0.8	0.101	0.002	2849	305	22.5	2.0	0.79	−2.77
THG5-DUP	Disseminated	0.5076	20.2	0.4	0.131	0.009	0.033	0.004	12.7	0.3	0.099	0.007	2980	369	22.8	2.8	0.84	−3.63
THG4	Massive	0.5068	11.6	0.3	0.327	0.007	0.134	0.005	7.3	0.2	0.193	0.005	416	19	10.9	0.5	0.64	7.21
THG4-DUP	Massive	0.5044	11.8	0.9	0.336	0.005	0.137	0.005	7.4	0.5	0.200	0.007	415	34	11.0	0.5	0.29	7.32
THG9	Massive	0.5132	17.9	0.5	0.216	0.005	0.058	0.002	11.3	0.3	0.157	0.005	1478	69	20.3	0.9	0.59	7.19
THG9-DUP	Massive	0.5117	17.7	0.6	0.211	0.008	0.055	0.003	11.1	0.4	0.156	0.007	1545	98	21.3	1.2	0.58	7.60
THG7	Banded	0.5069	13.1	0.4	0.286	0.015	0.175	0.012	8.2	0.2	0.111	0.003	360	27	4.8	0.4	0.86	1.61
THG8	Banded	0.5123	10.7	0.4	0.129	0.002	0.060	0.003	6.7	0.3	0.069	0.003	854	53	8.6	0.5	0.54	1.03
THG10A	Banded	0.5167	19.3	0.2	0.185	0.008	0.062	0.007	12.2	0.1	0.123	0.002	1490	179	14.8	1.8	0.98	1.59
THG10A-DUP	Banded	0.5071	19.0	1.0	0.187	0.009	0.062	0.004	11.9	0.6	0.125	0.005	1477	117	15.2	1.0	0.61	2.10
THG10B	Banded	0.5101	14.3	0.7	0.129	0.006	0.039	0.005	9.0	0.5	0.090	0.002	1737	242	17.1	2.2	0.92	1.69
THG10B-DUP1	Banded	0.5173	15.0	0.6	0.133	0.004	0.040	0.003	9.4	0.4	0.093	0.003	1820	170	17.7	1.5	0.84	1.56
THG10B-DUP2	Banded	0.5149	14.3	0.7	0.124	0.003	0.037	0.002	9.0	0.4	0.087	0.002	1865	145	17.6	1.1	0.70	1.06

[a] Sample numbers ended with "DUP" indicate duplicate analyses of mineral separates from the same sample. "THG10A" and "THG10B" indicate fine-grained pyrite and coarse-grained pyrite from the same ore specimen THG10, respectively.
[b] Results are blank corrected. Blanks for Re and Os were 6.4 ± 1.1 pg and 2.0 ± 0.4 pg, respectively, with an average $^{187}Os/^{188}Os$ value of 0.70 ± 0.11 (1σ, n = 5).
[c] Uncertainty correlation factor (rho) is applied to assess the degree of correlation between $^{187}Re/^{188}Os$ and $^{187}Os/^{188}Os$ ratios (Ludwig, 1980).
[d] Initial $^{187}Os/^{188}Os$ ratios are calculated using an age of 530 Ma afforded by isochron plots of $^{187}Re/^{188}Os$ and $^{187}Os/^{188}Os$ ratios for both the massive and banded ores.

trace elements of magnetite were determined by LA-ICP-MS. Detailed analytical procedures are described in Appendix A.

4.1. Re–Os isotopes

Eight samples are selected for pyrite separation and include disseminated ores (Fig. 3a), massive ores (Fig. 3b), and banded ores (Fig. 3c and d). According to the occurrence of pyrite (Fig. 3c), fine-grained pyrite disseminated in ore (THG10A) and coarse-grained pyrite infilled in ore (THG10B) are separated from the same sample. A total of sixteen analyses are obtained and are listed in Table 1.

Pyrite separates from the Tianhu Fe deposit have 10.7 to 54.7 ppb Re, 0.124 to 0.364 ppb total Os, and 0.033 to 0.175 ppb common Os (Table 1). All samples have low $^{187}Re/^{188}Os$ (360 to 4216) and $^{187}Os/^{188}Os$ ratios (4.8 to 33.7). Uncertainty correlation factors (rho) between $^{187}Re/^{188}Os$ and $^{187}Os/^{188}Os$ ratios range from 0.29 to 0.98. These pyrite samples contain significant amounts of common Os and are different from "LLHR" (low-level, highly radiogenic) sulfides as defined by Stein et al. (2000). Therefore, conventional isochron plots of $^{187}Re/^{188}Os$ versus $^{187}Os/^{188}Os$ ratios are used and uncertainty correlation factors are also considered in the regression analysis. Regression of four pyrite separates from two massive ores yields a model 1 isochron age of 535 ± 36 Ma (2σ, MSWD = 0.27; Fig. 6a), with an initial $^{187}Os/^{188}Os$ ratio of 7.22 ± 0.49. Regression of seven pyrite separates from three banded ores yields an identical model 1 isochron age of 528 ± 18 Ma (2σ, MSWD = 1.6; Fig. 6b), with an initial $^{187}Os/^{188}Os$ ratio of 1.55 ± 0.29. Four analyses are plotted off the isochrones (Fig. 6c).

4.2. Chemical composition of magnetite

The mean contents of trace elements determined by LA-ICP-MS and standard deviation of the selected elements for each sample are summarized in Table 2 and detailed results are given in the Appendix B. In general, magnetite grains from the Tianhu Fe deposit have Mg, Al, Ti, V, Mn, Zn, and Ga contents ranging from ~5 to 3500 ppm, 100 to 1000 times their respective detection limits (Table 2). Chromium, Co, Ni, and Sn in magnetite are commonly 1 to 100 times the detection limits (~1 to 200 ppm) (Table 2), whereas Ca, Sc, Cu, Ge, Rb, Sr, Y, Zr, Nb, Mo, Ag, Cd, In, Ba, Hf, Ta, W, Pb, Bi, Th, and U are typically below or close to the detection limits (Appendix B).

As illustrated in Fig. 7, trace element contents in magnetite vary less than two orders of magnitude. Magnetite from the sample THG8 has the highest Mg, Mn, and Co contents, whereas magnetite from two samples THG1 and THG4 have higher Ga and lower Sn contents than others. Compositional variations between different magnetite samples can be further identified by binary plots of selected elements (Fig. 8). In general, there are no obvious differences in trace element contents of magnetite among disseminated, massive, and banded ores. For individual sample, almost all the samples show a well positive correlation between Mg and Al, whereas sample THG8 shows a weakly negative correlation between these elements (Fig. 8a). Magnesium also correlates positively with Mn for most samples (Fig. 8b). Aluminum shows a weakly positive correlation with Mn for most samples (Fig. 8c). In the plots of Al vs. Mn and Al vs. Ti, trace elements of magnetite define four separated fields (Figs. 8c and d). Samples THG1, 5, 9, and 10 show a good correlation between V and Ti (Fig. 8e). There is no obvious correlation of V and Cr except for the sample THG4 (Fig. 8f). Zinc shows a weakly positive correlation with Mn (Fig. 8g). Magnetite grains are divided into four groups in terms of different Mn and Ga contents (Fig. 8h).

4.3. Sulfur isotope

Analytical results for pyrite and pyrrhotite from the Tianhu Fe deposit are summarized in Table 3 and plotted in Fig. 9. Generally,

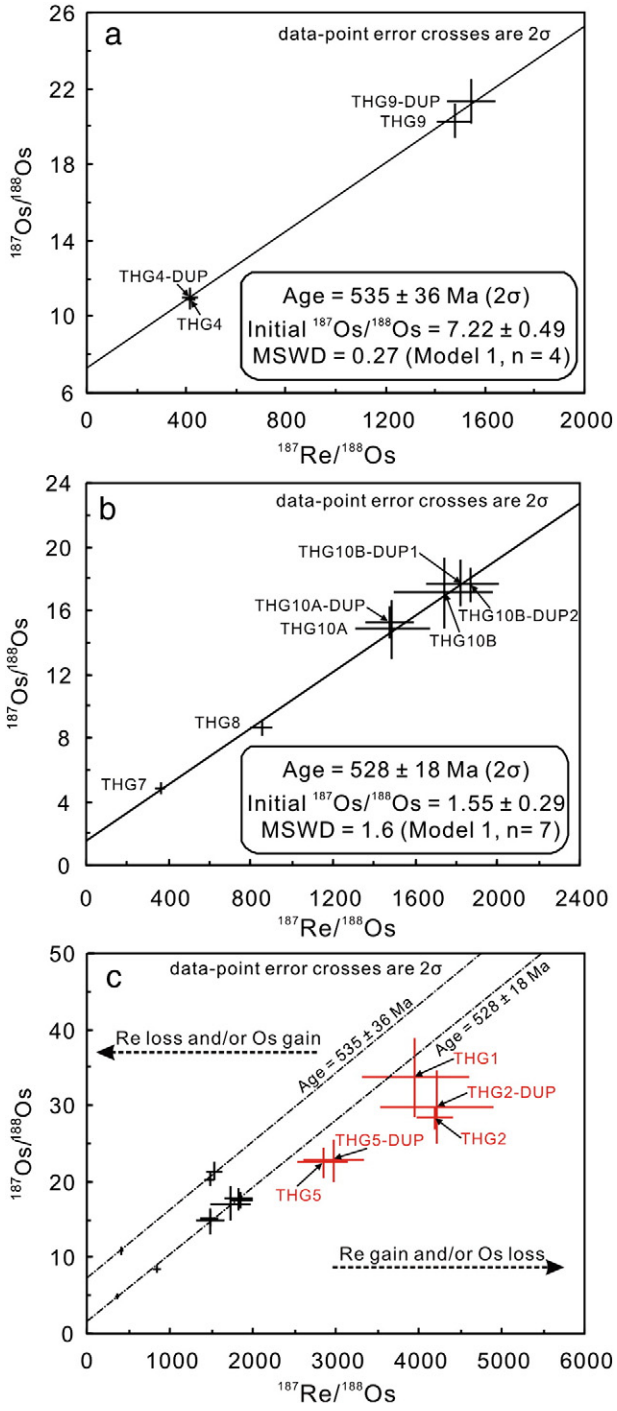

Fig. 6. Isochron plots of $^{187}Re/^{188}Os$ vs. $^{187}Os/^{188}Os$ for pyrite separates from massive ores (a) and banded ores (b), and scatter diagram for all analyses showing the behavior of Re–Os decoupling (c). Isochron ages are calculated using $^{187}Re/^{188}Os$ ratios, $^{187}Os/^{188}Os$ ratios, and uncertainty correlation factor (rho) between them by Isoplot/Ex, Ver. 3.23 (Ludwig, 2003).

sulfides have variable sulfur isotopic composition ($\delta^{34}S_{CDT}$) ranging from about −9.2 to +11.1‰ (Fig. 9). Most samples have $\delta^{34}S_{CDT}$ values clustering between +6 and +12‰. There are no obvious differences in $\delta^{34}S_{CDT}$ values for different ore types (Table 3). Fine-grained (THG10A) and coarse-grained (THG10B) pyrite separates from the same ores have similar $\delta^{34}S_{CDT}$ values of −0.47‰ and −0.78‰, respectively.

4.4. Trace elements of pyrite

Pyrite from the Tianhu Fe deposit typically contains relatively high Co (346–3274 ppm) and Cu (149–2695 ppm), moderate Cr, Ni, Zn, Pb, As, and Mo (1.9–127 ppm), and low Ag, Ga, Ge, Y, Zr, Nb, Sn, Sb, La, Ce, Bi, Th, and U (from <0.1 to 33 ppm) (Table 4). Pyrite from the disseminated ore, THG1, has the highest trace element contents, particularly Co, Cu, Mo, and Pb. Fine-grained pyrite (THG10A) from the ore THG10 has lower Cu, Y, Sb, La, Ce, and Pb than coarse-grained pyrite (THG10B) from the same ore. All pyrite samples have Co/Ni ratios ranging from ~10 to 270. Most pyrite samples have Co contents similar to those from volcanogenic and hydrothermal deposits, but have lower Ni contents (Fig. 10). In the Co–Ni correlation diagram (Bajwah et al., 1987; Brill, 1989), all the samples are obviously different from sedimentary and magmatic deposits and plot in the field of volcanogenic field with lower Ni contents (Fig. 10).

5. Discussion

5.1. Origin of the Tianhu deposit

The Tianhu deposit was first considered as a magnesian skarn deposit (BNGEXUAR, 1976; Luo and Zhu, 1986; Zhang, 1985; Zhao, 1989) because large skarn alteration zones occur in the bottom of orebodies with a mineral assemblage of forsterite, tremolite, diopside, actinolite, and serpentine. The deposit was also thought to be a sedimentary deposit with hydrothermal overprint (Chen, 2007; Jia, 1991; Song et al., 1989). The debate is centralized on the derivation of the ore-forming fluids from sedimentary strata, magmatic hydrothermal process, or both.

The orebodies and ores display sedimentary features even if the Tianhu deposit was subjected to deformation, metamorphism, and migmatization. For example, orebodies occur as stratified or stratoid beds in the dolomitic marble of the Tianhu Group. Dolomites from the ores and dolomitic marble have a carbon and oxygen isotope composition similar to that of marine carbonates (Song et al., 1989). Some ores exhibit laminated to banded structures (Fig. 3b and c). Moreover, ore and gangue minerals also show oriented arrangement. Magnetite and pyrite bands are approximately parallel to biotite and dolomite grains (Fig. 4c and d). These relict sedimentary structures or textures indicate that the ores may have been originally deposited by a sedimentary process. Trace element composition of magnetite also reveals a sedimentary origin of magnetite. Most magnetite grains have Ca + Al + Mn and Ti + V contents (Fig. 11) similar to those of banded iron formation (BIF), indicating the derivation of sedimentary process.

However, the pure sedimentary origin cannot be supported by trace element composition of magnetite. In general, all the magnetite grains have similar trace element patterns normalized to the bulk continental crust (Fig. 7), indicating that they may share a common source. However, the absence of obvious variation trends of trace element pairs for all magnetite grains cannot be explained by a single fluid evolution process. For example, magnetite grains from the sample THG8 contain significantly high Mg and Mn but low Al than those from other samples (Fig. 8a–c), inconsistent with the synchronous decrease of all trace elements if the same fluids evolve from early to late (e.g. from high temperature to low temperature). The higher Mg, Mn, and Ti but lower Al contents in magnetite grains from sample THG8 are possibly due to selective metasomasis which has added Mg, Mn, and Ti but discarded Al. This suggestion is consistent with the fact that the ilmenite, talc, and magnesite were enclosed in the magnetite grains (Fig. 4h). No obvious differences in trace elements of magnetite grains among disseminated, massive, and banded ores indicate the complexity of fluid evolution. Even for magnetite grains from the same type of ores such as massive ores, THG4, THG6, and THG9, trace elements of magnetite also define different fields in the

Table 2
LA-ICPMS results for trace elements (in ppm) in magnetite from the Tianhu Fe deposit.

		Mg	Al	Ti	V	Cr	Mn	Co	Ni	Zn	Ga	Sn
DL[a]		1.5	0.82	1.0	0.20	2.1	1.6	0.036	1.1	0.64	0.046	0.74
THG1	ave (n = 9)[b]	95	508	517	532	68.1	185	8.5	3.5	63.1	22.1	1.14
	stdev	24	80	105	49	95.5	23	2.6	0.8	15.0	7.1	0.28
THG2	ave (n = 17)	270	77	48	161	3.1	497	2.8	5.3	177	4.2	2.96
	stdev	53	20	10	6	0.5	35	2.6	1.5	52	1.0	1.00
THG4	ave (n = 15)	177	290	338	351	16.7	178	3.6	1.66	74	19.7	3.4
	stdev	41	60	106	110	7.1	16	2.6	0.45	15	3.5	0.3
THG5	ave (n = 17)	389	291	501	298	4.3	156	0.99	15.0	79	5.4	9.5
	stdev	113	86	65	39	2.8	34	0.69	4.6	28	0.3	5.9
THG6	ave (n = 19)	319	124	144	170	5.0	405	6.1	2.18	56	4.4	12.4
	stdev	41	22	10	8	2.6	18	1.9	0.83	13	0.4	4.6
THG7	ave (n = 9)	534	187	271	202	28.6	196	0.35	1.54	65.8	5.0	16.4
	stdev	137	25	21	8	17.7	50	0.17	0.95	19.4	0.4	8.0
THG8	ave (n = 4)	3585	59	545	205	7.4	1656	14.9	2.76	97	4.8	13.5
	stdev	886	37	91	22	0.9	124	3.20	0.64	36	0.9	3.8
THG9	ave (n = 7)	453	194	120	144	3.4	197	1.32	1.84	81	7.0	12.2
	stdev	40	52	19	38	0.8	19	0.63	0.58	16	0.6	2.3
THG10	ave (n = 18)	463	225	148	162	4.7	158	0.99	3.41	95.5	6.37	15.8
	stdev	77	66	24	55	1.6	16	0.55	1.54	22.8	0.30	8.9

Abbreviation: D.L. = detection limit, ave = average, stdev = standard deviation.
[a] Detection limit (D.L.) = $3 \times \sigma^{i}_{background} \times C^{i}_{RM}/cps^{i}_{RM}$, where $\sigma^{i}_{background}$ is the standard deviation of multiple determinations of element *i* in the background, C^{i}_{RM} and cps^{i}_{RM} are concentration and peak intensity of element *i* in the reference material, respectively.
[b] Numbers in parenthesis represent the number of analyzed spots.

binary plots (Fig. 8), also indicating the extremely complex fluid evolution. In the Ca + Al + Mn vs. Ti + V diagram (Fig. 11), some magnetite grains plot in the center or margin of "iron oxide–copper–gold (IOCG) deposits" field, indicating they were probably formed from a later hydrothermal event.

5.2. Origin of pyrite

The Re–Os isotopes of pyrite from the Tianhu Fe deposit provide important constraints on not only mineralization age but also possible metal sources. Isochron diagrams for massive and banded ores yield initial Os isotope ratios of 7.22 ± 0.49 and 1.55 ± 0.29, respectively. These ratios are much more radiogenic than the chondritic $^{187}Os/^{188}Os$ ratio of 0.12 at 530 Ma, indicating that the source of Os, by inference, other ore materials are mainly crust-derived. Although Re–Os dating of pyrite separates showed that massive and banded ores have formed almost simultaneously, they have different initial Os isotope ratios and sulfur isotopes (Fig. 12). Pyrite from massive ores has more radiogenic initial Os isotope ratios and is richer in heavy sulfur isotopes than those from banded ores (Fig. 12), indicating that they probably experienced different ore-forming processes. Pyrite from sample THG8 has similar initial Os isotope ratios to those from the other banded ores, but has heavier sulfur isotope composition, indicating that this sample may have been modified by low radiogenic Os but heavy sulfur-enriched fluids. Pyrite separates from ores THG1, 2, and 5 plot off the isochron defined by those from other ores (Fig. 6c), showing open behavior of Re–Os systematic. It's worthy noting that magnetite grains from almost the same ores show IOCG affinity in terms of their trace element

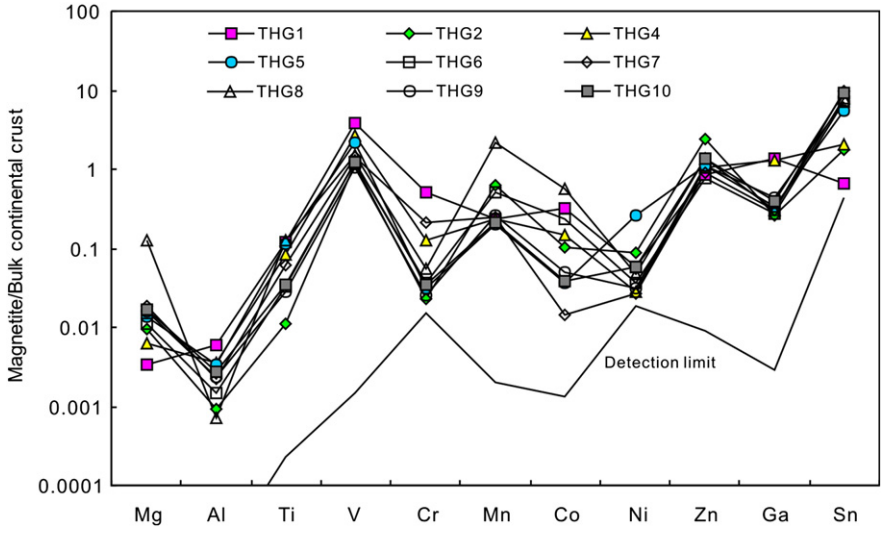

Fig. 7. Multi-element variation diagram of the median trace element concentrations in magnetite normalized to bulk continental crust (Rudnick and Gao, 2003).

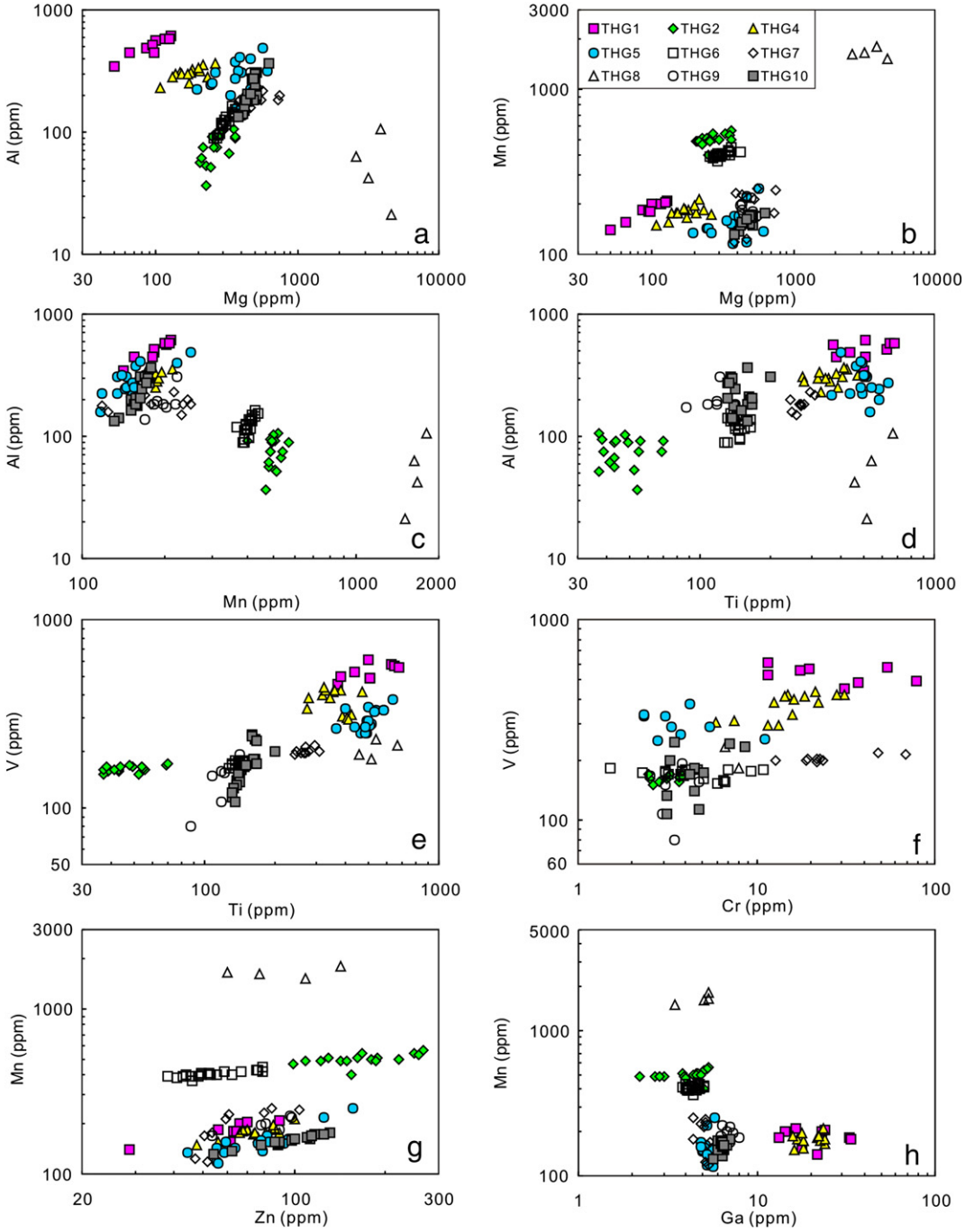

Fig. 8. Binary plots of selected trace elements in magnetite from the Tianhu Fe deposit.

composition. The good coupling between pyrite Re–Os isotopes and magnetite trace elements of the same ores indicate that these ores may have suffered from hydrothermal modification.

The remobilization of ores was also supported by trace element and sulfur isotope composition of pyrite. Pyrite from the Tianhu deposit has Co contents similar to those of volcanogenic and hydrothermal deposits, but obviously higher than pyrite from sedimentary deposits (Fig. 10). Some pyrite samples have Co/Ni ratios similar to volcanogenic deposits, but other samples have elevated Co/Ni ratios due to extremely low Ni contents (Fig. 10). The depleted Ni contents in pyrite were probably attributed to metamorphic conversion of pyrite to pyrrhotite because Co is concentrated in pyrite while Ni does so in pyrrhotite (Campbell and Ethier, 1984; Loftus-Hills and Solomon, 1967). However, the composition of pyrite cannot be significantly altered even under high grade metamorphic conditions, except under particular circumstances involving hydrothermal remobilization (Bralia et al., 1979). Moreover, microscopic observations show that pyrrhotite accounts for only a small proportion of sulfides and pyrite is dominant (Fig. 4e). Therefore, hydrothermal remobilization rather than mineral transformation may account for the low Ni contents of pyrite.

Table 3
Sulfur isotopic composition of sulfides from the Tianhu deposit, NW China.

Sample no.[a]	Ore type	Mineral	$\delta^{34}S_{CDT}$ (‰)	Reference
THG1	Disseminated	Pyrite	10.31	This study
THG2	Disseminated	Pyrite	10.96	This study
THG5	Disseminated	Pyrite	−9.23	This study
THG4	Massive	Pyrite	8.15	This study
THG9	Massive	Pyrite	5.93	This study
THG7	Banded	Pyrite	−0.86	This study
THG8	Banded	Pyrite	7.62	This study
THG10A	Banded	Pyrite	−0.47	This study
THG10B	Banded	Pyrite	−0.78	This study
T1	Unknown	Pyrite	10.98	IGCAS, 1976
T2	Unknown	Pyrite	8.31	IGCAS, 1976
T3	Unknown	Pyrite	10.19	IGCAS, 1976
T4	Unknown	Pyrite	11.07	IGCAS, 1976
T5	Unknown	Pyrite	7.69	IGCAS, 1976
T6	Unknown	Pyrrhotite	10.35	IGCAS, 1976

[a] "THG10A" and "THG10B" indicate fine-grained pyrite and coarse-grained pyrite from the same ore specimen THG10, respectively.

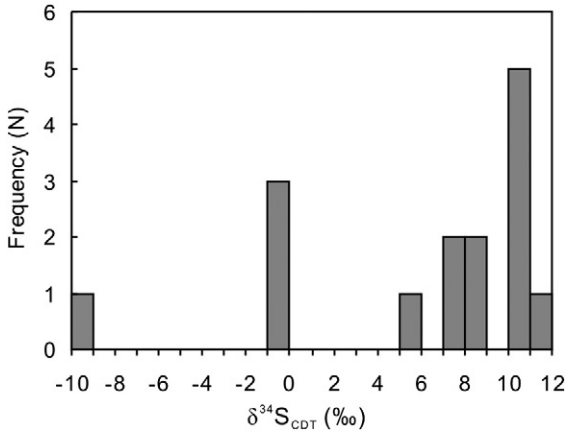

Fig. 9. Histogram of sulfur isotopic composition of sulfides from the Tianhu Fe deposit.

Large variations of $\delta^{34}S$ values (−10 to +12‰) of sulfides from the Tianhu deposit argue against a single sedimentary or hydrothermal origin of sulfur (Velasco et al., 1998). Most sulfides have $\delta^{34}S$ values clustering between +6‰ and +12‰, indicating derivation from marine sulfates. Although no sulfur isotope data of marine sulfates are available in the study area, $\delta^{34}S$ values of marine evaporites in the Proterozoic strata are estimated as +17‰ (Claypool et al., 1980). Bacterial sulfate reduction can produce sulfate–sulfide fractionations that typically range from 15 to 60‰ (Goldhaber and Kaplan, 1982), whereas those associated with abiotic thermochemical reactions with organic compounds range from zero to as much as 10‰ (Kiyosu, 1980; Orr, 1974). Therefore, the negative $\delta^{34}S$ values of pyrite indicate that part of sulfur probably has derived from bacterial sulfate reduction of marine sulfates, whereas those positive values may indicate complete reduction of the original sulfates either by bacterial or thermochemical sulfate reduction processes. Some sulfides have $\delta^{34}S$ values close to zero, indicating that sulfur may have derived from bacterial reduction of sulfates. However, the process involving magmatic or hydrothermal activity cannot be excluded because contemporary granitic magmatism (ca. 543 Ma) (Song et al., 1989) was also indentified in this area. Therefore, the sulfur, by inference, the iron, is most likely to derive from the replacement of sulfates in the Precambrian strata by a hydrothermal fluid.

5.3. Timing of Fe mineralization

There are two different views about the age of the Tianhu Fe deposit (Li and Chen, 2003). The deposit was considered to have a Neoproterozoic age similar to that of the hosting metamorphic rocks because orebodies appear in bedded or near-bedded shapes parallel to the stratum (Chen, 2007). Magnetite ores and amphibolites have Nd model ages between ~1266 and 892 Ma with an average age of ~1007 Ma, which was interpreted as the maximum formation age of the Tianhu Fe deposit (Li and Chen, 2003). Others argued that the deposit was formed in Late Carboniferous or Early Permian and was closely related to contemporaneous intrusions of granites (Zhao, 1989).

Table 4
Selected trace element contents (ppm) of pyrite from the Tianhu deposit, NW China.

Sample no.	THG1	THG2	THG4	THG5	THG7	THG8	THG9	THG10A[a]	THG10B[a]
Cr	21.1	18.9	22.5	19.9	19.4	19.3	22.5	19.6	21.1
Co	3274	553	1979	346	1143	1090	874	647	1222
Ni	33.3	19.1	7.25	35.4	6.68	16.8	5.63	14.3	7.05
Cu	2695	482	154	281	396	149	413	275	647
Zn	86	61	27.2	34	118	40	92	56	127
Ga	0.23	0.21	0.23	0.14	0.16	0.12	0.15	0.15	0.29
Ge	0.59	0.62	0.50	0.43	0.47	0.46	0.66	0.58	0.55
As	5.9	4.8	19.4	2.61	6.4	8.0	10.8	6.0	3.8
Y	0.94	0.35	0.39	0.086	0.12	0.070	0.095	0.081	0.59
Zr	5.5	2.61	1.02	1.32	0.96	0.44	1.77	1.05	0.45
Nb	0.27	0.85	0.12	0.048	0.020	0.031	0.41	0.059	0.043
Mo	43	18.5	6.9	4.2	3.4	1.85	3.3	4.9	2.07
Ag	1.57	33	0.10	4.77	30.6	6.76	0.81	10.0	0.59
Sn	1.68	1.13	0.69	3.9	1.80	0.71	1.08	1.96	1.19
Sb	2.42	1.01	1.05	1.35	1.18	0.91	1.37	1.23	5.2
La	0.69	1.98	0.45	0.066	0.16	0.031	0.052	0.11	0.85
Ce	1.42	3.14	0.91	0.13	0.32	0.060	0.13	0.25	1.54
Pb	28.5	18.4	10.5	13.2	16.2	9.4	10.7	10.8	79
Bi	2.85	1.32	1.23	0.85	1.95	0.85	1.26	0.91	1.01
Th	0.13	0.64	0.024	0.57	0.62	0.033	0.86	2.53	0.25
U	0.51	1.07	0.072	0.96	0.52	0.031	0.56	1.62	0.45
Co/Ni	98	29	273	9.8	171	65	155	45	173

[a] "THG10A" and "THG10B" indicate fine-grained pyrite and coarse-grained pyrite from the same ore specimen THG10, respectively.

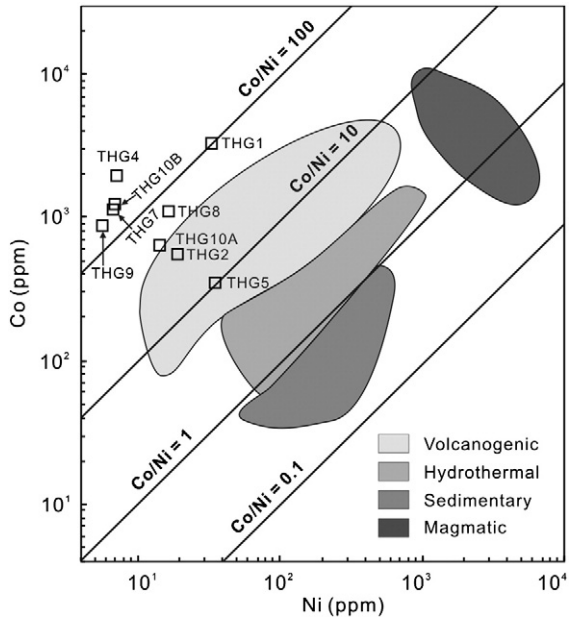

Fig. 10. Co–Ni concentration plot of pyrite from the Tianhu Fe deposit. "THG10A" and "THG10B" represent fine-grained pyrite and coarse-grained pyrite in the same ore specimen, respectively. Reference fields for different types of deposits or geological environments are defined according to Co and Ni values from Bajwah et al. (1987) and Brill (1989).

Pyrite Re–Os isotope ages first provide important constraints on the timing of sulfide formation. Pyrite separates from the massive and banded ores have a similar Re–Os age of ca. 530 Ma. Pyrite is commonly associated with magnetite in the banded ores or occurs as veins infilling in the massive ores, indicating that pyrite and magnetite were formed almost simultaneously or pyrite was formed later than magnetite. But the age of pyrite cannot be interpreted to the mineralization of magnetite, because the volcanic rather than sedimentary origin of pyrite contradicts the sedimentary environment of the host carbonate rocks which were metamorphosed to dolomitic marble. We therefore interpret the Re–Os age of pyrite as the time of a later hydrothermal mineralization event after the formation of the Tianhu Fe deposit. Although the contemporary tectono-thermal event was not widespread in the Tianhu area, ca. 534 Ma granitoid intruding the Tianhu Group was reported (Hu et al., 1986).

Although no isotope data is available for the timing of magnetite mineralization, the deposit was proposed to be syngenetic with the sedimentary carbonate rocks or metamorphosed equivalents (Chen, 2007). The minor remained siderite bodies in the western part of the main magnetite bodies may be another supporting evidence (Song et al., 1989). We thus also believe the original Fe mineralization was nearly contemporary with the sedimentary diagenesis in Neoproterozoic. Because the Tianhu Fe deposit has experienced complex geological events, multiple stages of mineralization also cannot excluded.

5.4. Open behavior of the Re–Os isotopic system

The isochron diagram demonstrates that some of pyrite separates show open system behavior of Re–Os isotopes by the process of Re gain and/or Os loss (Fig. 6c). Re–Os isotopic system can be perturbed by a variety of processes such as hydrothermal or supergene alteration, deformation, and metamorphism (Lambert et al., 1998; Morelli et al., 2004; Ruiz and Mathur, 1999; Tristá-Aguilera et al., 2006).

The Tianhu deposit has undergone extensive deformation and contact metamorphism after the deposition of magnetite. For example, orebodies are locally brecciated and rounded to smooth tectonic lens due to the late tectonic activity. Some ores are crosscut by late pyrite and dolomite veins, forming the brecciated structure (Fig. 3d). The well rounded pyrite also indicates tectonic transformation (Fig. 4b). Re–Os isotope data of pyrite separates for intensively deformed ores (THG1), show a little scatter below the ~528 Ma isochron of banded ores (Fig. 6c), indicating that deformation process may not significantly alter the Re–Os isotope systematic. However, pyrite separates from weakly tectonised disseminated ores (THG2 and THG5) have much scatter below the ~528 Ma isochron (Fig. 6c), providing evidence that Re can be gained or Os can be lost as a result of certain processes except deformation effects.

In addition to deformation and metamorphism, hydrothermal or supergene processes can also redistribute Re and/or Os. Experimental studies have demonstrated that Re can only be remobilized by very oxidized hydrothermal fluids under high-temperature (above 400 °C) conditions (Xiong and Wood, 1999; Xiong et al., 2006) and

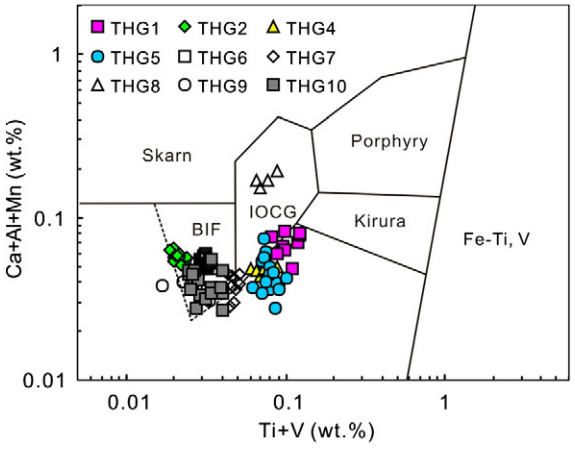

Fig. 11. Plot of Ca + Al + Mn vs. Ti + V for LA-ICP-MS data of magnetite from the Tianhu deposit. Because Ca content of magnetite is lower than the detection limit (~156 ppm), Ca content is calculated using zero ppm. Reference fields are after Dupuis and Beaudoin (2011). BIF: banded iron formation, Skarn: Fe–Cu skarn deposits, IOCG: iron oxide–copper–gold deposits, Porphyry: porphyry Cu deposits, Kiruna: Kiruna apatite–magnetite deposits, Fe–Ti, V: magmatic Fe–Ti-oxide deposits.

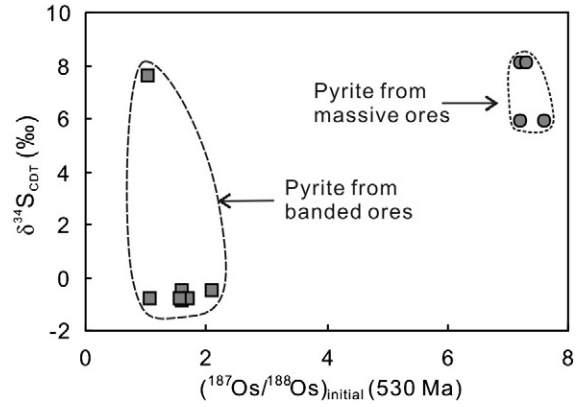

Fig. 12. Plot of $\delta^{34}S_{CDT}$ values versus initial $^{187}Os/^{188}Os$ ratios showing different sulfur and osmium isotope compositions for pyrite separates from massive and banded ores.

disturbance of Re–Os systematics will not be severe as long as low-temperature (100–200 °C) hydrothermal alteration is restricted to oxygen fugacity conditions under which sulfide is stable (Xiong et al., 2006). As described above, the host strata of the Tianhu Group was intruded by Early Paleozoic granitoids. ~528 Ma pyrite is older than ~460 Ma granitoids, indicating that some pyrite samples may also have suffered from the modification related to granitic magmatism. Therefore, the open-system behavior of Re–Os isotopes of part of pyrite separates from the Tianhu deposit is most likely to result from high-temperature hydrothermal alteration after ore formation.

6. Conclusions

Pyrite separates of Fe ores from the Tianhu Fe deposit have a Re–Os isochron age of ~530 Ma, which was interpreted to be post-ore hydrothermal timing for sulfide formation. Magnetite at Tianhu was derived from sedimentary process overprinted by hydrothermal activity. Sulfur isotopic composition of pyrite reveals that the sulfur was likely to derive from marine sulfate reduction either by bacterial or thermochemical processes. Trace element composition of pyrite indicates hydrothermal remobilization of ores. Therefore, the Tianhu Fe deposit may be a hydrothermal overprint sedimentary type deposit. Re–Os isotope of sulfides was a good indicator for post-ore process.

Acknowledgments

This work was jointly supported by grants from the Chinese 973 project (2012CB416804) and the "CAS Hundred Talents" Project (KZCX2-YW-BR-09) from the Chinese Academy of Sciences. Zhihui Dai, Ning An, and Wenqin Zheng are thanked for their assistance with LA-ICP-MS, sulfur isotope, and electron probe analyses at IGCAS (Guiyang). Two anonymous reviewers, Prof. Franco Pirajno and Prof. Rucheng Wang are thanked for their constructive comments and suggestions which have significantly improved the manuscript.

Appendix A. Summary of analytical methods

A.1. Re–Os isotopes

Re–Os isotope analyses were performed at the State Key Laboratory of Ore Deposit Geochemistry, Institute of Geochemistry, Chinese Academy of Sciences (IGCAS). Samples of approximately 0.1 to 0.5 g of pyrite were accurately weighed and loaded into a 120 ml Carius tube with known amounts of ^{185}Re and ^{190}Os spikes (Shirey and Walker, 1995). Samples were digested and equilibrated using 10–20 ml of concentrated HNO_3 and 2 ml of HCl at 200 C for about 12 h. Osmium was separated as OsO_4 from the matrix using the in-situ distillation equipment, whereas Re was separated from the remaining solution after Os distillation using the anion exchange resin (Biorad AG 1 × 8, 200–400 mesh) technique (Qi et al., 2007, 2010).

Rhenium and Os were determined by a PE ELAN DRC-e ICP-MS. Procedural blanks are 6.4 ± 1.1 pg and 2.0 ± 0.4 pg, respectively, with an average $^{187}Os/^{188}Os$ value of 0.70 ± 0.11 (1σ, $n = 5$). Absolute uncertainties (2σ) are derived from error propagation of uncertainties in Re and Os mass spectrometer measurements, blank abundances and isotopic compositions, spike calibrations. To monitor long-term mass spectrometry reproducibility, in-house standard solutions of Re and Os were analyzed repeatedly. The Re standard (~1 ppb) yielded an average $^{187}Re/^{185}Re$ ratio of 1.697 ± 0.031 (1σ, $n = 10$), whereas the Os standard (~50 pg/g) yielded an average $^{187}Os/^{188}Os$ ratio of 0.117 ± 0.003 (1σ, $n = 10$). The duplicate analyses of the same sample also show good short-term reproducibility (Table 1). Iridium was added to the Re- and Os-bearing solutions for mass discrimination correction as proposed by Schoenberg et al. (2000) for Re. The analytical results of Chinese national Re–Os reference materials, JCBY (Cu–Ni sulfides) and RCOR (cobalt-rich ferromanganese crusts) were in good agreement with the certified values (Huang et al., 2013a,b,c).

A.2. Chemical composition of magnetite

Major and trace elements of magnetite were determined by a Coherent GeoLasPro 193 nm Laser Ablation system coupled with an Agilent 7700× ICP-MS at the State Key Laboratory of Ore Deposit Geochemistry, IGCAS. Detailed operating conditions for the laser ablation system and the ICP-MS instrument and data reduction are described in Liu et al. (2008). Helium was applied as a carrier gas and argon was used as the make-up gas and mixed with the carrier gas via a T-connector before entering the ICP. Each analysis includes a background acquisition of approximately 20 s (gas blank) followed by 40 s of data acquisition from the sample. Analytical spots (60 μm) were ablated by 160 successive laser pulses (4 Hz). Element contents were calibrated against multiple-reference materials (GSE-1G, BCR-2G, BIR-1G, BHVO-2G and NIST610) using ^{57}Fe as an internal standard (Gao et al., 2013). Every 8 sample analyses were followed by one analysis of GSE-1G as a quality control to correct the time-dependent drift of sensitivity and mass discrimination. Off-line selection and integration of background and analyte signals, and time-drift correction and quantitative calibration were performed by *ICPMSDataCal* (Liu et al., 2008).

A.3. Sulfur isotopes

Sulfur isotopes were analyzed using a EuroVector EA3000 element analyzer (EA) coupled to a GV IsoPrime isotope ratio mass spectrometer at the State Key Lab of Environmental Geochemistry, IGCAS. Appropriate amounts of powdered sulfide separates were weighed and packed in tinfoil. Sulfur in sulfide minerals was converted to SO_2 for isotopic analysis by burning in the reactor under a constant temperature of about 1000 °C using a stream of purified oxygen. The sulfur dioxide was then carried by helium into the mass spectrometer. The sulfur isotopic compositions are expressed using the delta per mil notation ($\delta^{34}S$) with respect to Vienna Canyon Diablo Troilite (V-CDT). Repeated analyses of national Ag_2S standards GBW04414 and GBW04415 yielded $\delta^{34}S$ values of −0.07 ± 0.09‰ (1σ, n = 27) and 22.33 ± 0.09‰ (1σ, n = 3), respectively, in good agreement with the certified values of −0.07 ± 0.13‰ and 22.15 ± 0.14‰ (1σ) (Ding et al., 2001).

A.4. Trace elements of pyrite

Trace element contents of pyrite were determined by a PE ELAN DRC-e ICP-MS at the State Key Laboratory of Ore Deposit Geochemistry, IGCAS. The detailed method was described by Qi et al. (2000). Fifty milligrams of pyrite powder was accurately weighed and placed in a PTFE bomb. About 1 ml of concentrated HNO_3 was added for each sample. The bombs were then placed on a hot plate, and the solutions were evaporated to dryness to remove most of sulfur. One milliliter of HF and 0.5 ml of HNO_3 were then added. The sealed bombs were then placed in an electric oven at 190 °C for 12 h. After cooling, the solutions were evaporated to dryness on a hot plate at about 150 °C followed by the addition of 1 ml of HNO_3 and again evaporation to dryness. The residues were re-dissolved by adding 8 ml of 40% (v/v) HNO_3, and 1 ml of 0.5 μg ml^{-1} Rh solution was also added as an internal standard. The bombs were re-sealed and placed in the electric oven at 140 °C for about 4 h. After cooling, 0.4 ml of the resulting solution was diluted to 10 ml using Millipore water. The final solution was used for ICP-MS analyses. Precisions were typically better than 5% RSD (relative standard deviation).

Appendix B. Full analytical results (in ppm) for laser ablation ICP-MS of magnetite from the Tianhu Fe deposit, northwestern China

Spot no.	Mg	Al	Ti	V	Cr	Mn	Co	Ni	Zn	Ga	Sn
Detection limit	1.45	0.82	1.01	0.2	2.08	1.58	0.036	1.07	0.64	0.046	0.74
THG1–01	99	556	370	455	31.4	203	9.34	4.08	66.9	14.4	b.d.l
THG1–02	85	486	440	532	11.5	184	3.83	3.46	56.2	13.4	1.39
THG1–03	127	611	509	490	37.5	211	9.20	3.58	89.5	16.5	0.83
THG1–04	95	523	623	582	54.3	182	9.79	3.71	63.1	33.1	1.52
THG1–08	114	573	647	569	19.7	200	6.17	2.60	66.4	23.3	0.99
THG1–09	123	584	678	560	17.7	208	7.80	1.80	70.1	24.3	0.79
THG1–10	51	346	500	611	11.6	141	6.02	3.35	28.4	21.8	b.d.l
THG1–12	96	447	505	493	b.d.l	180	12.9	3.92	64.9	34.0	1.33
THG1–14	65	444	383	496	78.7	155	11.0	4.57	62.0	17.8	b.d.l
THG2–01	277	91	56	159	b.d.l	506	8.51	4.62	189	4.62	4.12
THG2–02	228	53	52	151	b.d.l	507	7.18	5.54	130	3.83	1.38
THG2–03	332	66	43	156	b.d.l	534	0.85	5.85	251	5.04	2.19
THG2–04	364	90	43	156	3.72	565	0.78	6.10	268	5.33	2.69
THG2–05	272	74	39	156	2.84	541	0.56	4.40	168	5.23	2.51
THG2–06	351	106	37	150	2.62	522	0.86	4.71	258	4.98	3.77
THG2–08	245	52	37	161	b.d.l	509	0.62	4.41	163	4.68	2.55
THG2–09	203	57	43	161	2.54	483	1.27	5.04	109	3.00	1.77
THG2–10	254	74	69	168	2.46	486	4.02	3.62	143	2.69	3.26
THG2–11	253	88	49	165	b.d.l	494	1.44	4.18	180	4.36	4.81
THG2–12	298	103	48	169	3.30	498	1.73	4.91	221	4.60	4.30
THG2–13	208	61	41	160	b.d.l	482	3.91	4.54	122	2.20	2.41
THG2–14	255	94	38	165	3.70	487	1.96	4.08	186	2.87	4.13
THG2–16	216	75	55	162	3.12	485	1.03	4.75	149	3.88	3.07
THG2–17	247	92	70	171	b.d.l	400	6.04	7.52	154	5.08	2.94
THG2–18	226	37	54	165	3.23	467	5.43	6.30	99.4	3.97	1.47
THG2–20	359	93	44	167	3.80	492	1.14	9.66	223	4.85	3.02
THG4–02	182	322	384	419	15.0	185	6.95	1.73	84.1	21.7	3.37
THG4–03	217	355	425	315	7.54	214	8.65	1.13	101	23.7	3.20
THG4–04	172	252	388	307	5.91	185	6.84	1.76	70.3	22.4	3.19
THG4–05	177	311	408	299	11.5	168	1.62	2.30	76.2	24.0	3.38
THG4–06	263	363	410	298	13.2	174	3.14	1.35	73.6	22.9	3.26
THG4–07	205	314	474	418	14.3	177	2.29	2.06	89.5	24.1	3.10
THG4–11	148	304	275	335	16.0	177	1.51	1.63	65.8	16.8	3.91
THG4–12	138	295	353	418	18.6	176	1.25	1.45	74.2	18.3	3.61
THG4–13	132	280	362	425	31.1	156	3.71	0.69	56.0	18.2	3.23
THG4–14	152	296	318	402	16.3	176	2.64	1.36	80.9	18.2	3.33
THG4–16	231	283	279	386	22.4	187	3.10	2.16	67.8	15.8	3.25
THG4–17	107	233	327	419	28.0	150	1.82	1.69	47.6	16.3	3.39
THG4–19	169	298	341	388	12.6	190	7.89	b.d.l	86.8	22.1	3.87
THG4–21	198	339	323	438	21.6	196	2.43	2.26	85.2	18.0	4.14
THG5–02	468	395	490	252	11.1	221	0.49	19.0	125	5.25	4.24
THG5–03	361	381	463	250	2.79	156	1.61	25.5	59.7	5.67	3.62
THG5–04	389	407	483	252	b.d.l	164	1.68	25.5	95.8	5.18	7.20
THG5–07	195	221	494	293	5.43	134	1.47	12.5	44.5	5.52	1.87
THG5–08	245	241	582	329	b.d.l	144	2.26	9.61	64.1	5.33	14.4
THG5–09	248	254	541	330	2.33	145	2.21	9.78	55.6	5.47	7.64
THG5–10	569	485	401	337	2.32	250	1.53	14.7	157	5.84	6.11
THG5–11	403	304	518	278	b.d.l	146	1.14	13.2	77.8	4.94	9.83
THG5–12	386	320	508	277	b.d.l	169	0.73	16.2	81.2	4.85	3.68
THG5–13	262	306	504	293	3.34	134	0.75	15.7	58.9	5.44	11.4
THG5–14	363	274	632	377	4.25	152	0.26	12.4	92.2	5.90	7.68
THG5–15	464	217	363	263	b.d.l	152	0.56	12.6	76.2	4.99	9.78
THG5–16	482	249	485	270	b.d.l	155	0.74	14.1	82.6	5.64	14.8
THG5–17	463	222	440	268	3.78	118	0.82	10.4	55.8	5.23	25.3
THG5–18	335	202	578	329	3.07	160	0.21	13.1	77.4	4.82	16.5
THG5–19	609	315	500	343	b.d.l	139	0.25	14.6	78.9	5.25	12.6
THG5–20	376	159	535	327	b.d.l	116	b.d.l	16.5	56.1	5.67	5.14

(*continued on next page*)

Appendix B (*continued*)

Spot no.	Mg	Al	Ti	V	Cr	Mn	Co	Ni	Zn	Ga	Sn
THG6–01	287	116	154	175	3.86	411	5.14	b.d.l	49.2	4.36	21.2
THG6–02	362	155	136	179	4.02	441	6.08	b.d.l	78.3	4.64	10.2
THG6–03	347	141	132	173	3.06	419	6.46	2.23	59.0	4.28	9.43
THG6–04	285	97	147	170	b.d.l	404	6.00	1.41	49.2	4.18	10.4
THG6–05	310	134	135	164	b.d.l	410	6.80	1.52	52.1	3.85	10.5
THG6–06	422	148	139	174	3.07	415	7.75	b.d.l	79.0	4.81	16.7
THG6–07	254	89	132	168	3.22	389	7.19	b.d.l	38.1	4.18	7.93
THG6–08	315	117	141	179	6.97	398	6.64	b.d.l	52.8	4.05	14.9
THG6–09	299	112	146	179	11.0	393	7.53	3.86	45.7	4.61	8.58
THG6–10	278	94	147	176	9.37	392	8.01	1.55	42.8	4.06	8.23
THG6–11	331	124	142	156	6.69	397	2.95	2.67	62.1	4.80	12.1
THG6–13	293	119	165	181	1.51	365	9.42	3.56	45.8	4.44	13.6
THG6–14	351	137	164	173	2.28	404	7.56	1.87	55.4	5.01	22.9
THG6–15	307	127	148	167	3.88	394	7.23	1.31	48.0	4.01	8.76
THG6–16	346	147	144	159	6.55	429	5.12	b.d.l	74.8	3.98	9.07
THG6–17	345	162	143	169	3.73	430	5.58	1.46	75.7	4.73	15.8
THG6–18	297	111	145	169	b.d.l	399	5.73	1.98	44.2	4.70	9.78
THG6–19	268	90	128	162	5.06	386	1.11	2.11	41.0	4.11	7.52
THG6–21	357	132	140	153	6.03	419	3.75	2.83	66.9	5.04	18.0
THG7–01	735	185	268	213	68.2	178	0.31	3.02	53.8	4.38	20.0
THG7–03	460	159	248	201	22.5	124	b.d.l	b.d.l	47.0	5.15	3.93
THG7–04	531	229	295	217	47.7	216	0.29	1.13	59.8	5.06	19.0
THG7–06	556	182	264	198	12.8	249	0.54	1.19	84.7	4.39	11.2
THG7–10	573	217	308	201	19.4	170	0.21	2.24	50.3	5.44	27.3
THG7–11	433	149	260	197	18.9	230	0.35	b.d.l	60.8	4.86	14.4
THG7–12	749	200	244	194	22.0	243	0.38	2.38	104	5.13	12.8
THG7–13	388	183	278	201	22.0	234	0.58	1.15	80.1	5.17	28.3
THG7–14	377	178	271	197	23.4	118	0.43	1.23	51.5	5.33	10.7
THG8–03	2631	64	539	232	6.71	1627	12.5	2.03	76.8	5.01	16.5
THG8–04	3140	42	455	193	b.d.l	1663	13.5	b.d.l	60.1	5.40	11.3
THG8–05	3914	107	671	215	b.d.l	1817	14.0	3.06	142	5.33	17.0
THG8–07	4652	21	514	182	8.02	1517	19.6	3.20	109	3.44	9.29
THG9–01	508	183	142	167	2.55	183	1.02	2.51	69.0	7.89	10.9
THG9–03	419	182	108	149	3.11	197	0.96	1.47	78.2	7.43	16.4
THG9–04	503	181	118	108	2.95	219	2.18	1.55	98.0	7.03	11.2
THG9–06	431	174	87	80	3.44	202	1.71	b.d.l	80.8	6.75	12.6
THG9–07	415	139	141	193	3.86	169	1.97	b.d.l	53.7	7.06	9.58
THG9–09	465	306	122	155	4.73	223	0.63	b.d.l	96.6	6.42	13.8
THG9–10	429	192	118	158	b.d.l	187	0.74	b.d.l	89.2	6.23	11.1
THG10–02	497	311	199	200	3.28	162	0.55	1.55	113	6.75	44.7
THG10–03	621	368	160	179	4.70	179	0.67	3.77	131	7.08	13.7
THG10–04	484	210	163	181	4.51	161	1.06	4.84	98.8	6.09	21.6
THG10–05	410	142	137	139	4.51	137	2.46	3.65	62.6	6.35	18.0
THG10–06	517	200	165	233	8.57	150	1.87	7.14	88.8	6.52	15.2
THG10–07	492	184	159	247	3.49	154	1.68	5.98	89.9	6.52	11.0
THG10–08	379	135	160	241	7.01	131	1.04	1.09	54.5	5.71	8.49
THG10–10	448	176	140	150	b.d.l	158	0.97	1.29	89.6	6.54	11.2
THG10–11	483	271	132	114	4.79	175	0.96	2.70	117	5.99	9.96
THG10–12	511	303	136	108	3.14	170	0.68	2.71	115	6.32	11.3
THG10–13	420	163	150	168	4.22	150	0.78	3.95	78.1	6.09	15.8
THG10–14	502	247	142	138	b.d.l	166	0.72	3.96	111	6.32	13.8
THG10–15	504	297	137	132	3.13	174	1.03	3.84	126	6.40	13.1
THG10–16	494	277	134	128	b.d.l	172	0.98	1.99	114	6.42	9.69
THG10–17	444	207	132	120	b.d.l	157	0.89	2.65	89.4	6.40	9.54
THG10–18	427	184	166	173	5.06	157	0.92	3.62	86.1	6.52	29.6
THG10–19	464	205	167	230	b.d.l	164	0.31	3.25	100	6.48	9.79

Abbreviation: b.d.l = below detection limit.

References

Bajwah, Z.U., Seccombe, P.K., Offler, R., 1987. Trace element distribution, Co:Ni ratios and genesis of the Big Cadia iron-copper deposit, New South Wales, Australia. Mineral. Deposita 22, 292–300.

Beaudoin, G., Dupuis, C., 2009. Iron-oxide trace element fingerprinting of mineral deposit types. In: Corriveau, L., Mumin, A.H. (Eds.), Exploring for Iron Oxide Copper–Gold Deposits: Canada and Global Analogues: GAC Short Course Notes, pp. 107–121.

BGMRXUAR, 1993. Regional Geology of Xinjiang Uygur Autonomous Region, Geological Memoirs, No. 32, Map Scale 1:500000. Geological Publishing House, Beijing, p. 1-841 (in Chinese).

BNGEXUAR, 1976. Preliminary discussion on the geological features and ore-forming conditions of Tianhu skarn iron deposit, Xinjiang province. Bureau of Nonferrous Geological Exploration of Xinjiang Uygur Autonomous Region. Episode of iron-copper mineral resources (No. 6)Geological Publishing House, Beijing, pp. 26–41, (in Chinese).

Bralia, A., Sabatini, G., Troja, F., 1979. A revaluation of the Co/Ni ratio in pyrite as geochemical tool in ore genesis problems. Mineral. Deposita 14, 353–374.

Brill, B.A., 1989. Trace-element contents and partitioning of elements in ore minerals from the CSA Cu–Pb–Zn deposit, Australia. Can. Mineral. 27, 263–274.

Campbell, F.A., Ethier, V.G., 1984. Nickel and cobalt in pyrrhotite and pyrite from the Faro and Sullivan orebodies. Can. Mineral. 22, 503–506.

Carew, M.J., 2004. Controls on Cu–Au mineralisation and Fe oxide metasomatism in the Eastern Fold Belt, NW Queensland, Australia. [Ph.D. thesis] James Cook University, Queensland.

Carroll, A.R., Graham, S.A., Hendrix, M.S., Ying, D., Zhou, D., 1995. Late Paleozoic tectonic amalgamation of northwestern China: sedimentary record of the northern Tarim, northwestern Turpan, and southern Junggar basins. Geol. Soc. Am. Bull. 107, 571–594.

Chen, S.P., 2006. Study on mineralization regularity and mineral resource assessment in Hami, Xinjiang. [Doctoral dissertation] Chinese Academy of Geological Sciences, Beijing, (in Chinese with English abstract).

Chen, Y.C., 2007. Research on large scale ore concentration area of strategic mineral resources in Xinjiang, China. Geological Publishing House, Beijing, (in Chinese with English abstract).

Chen, C.M., Lu, H.F., Jia, D., Cai, D.S., Wu, S.M., 1999. Closing history of the southern Tianshan oceanic basin, western China: an oblique collisional orogeny. Tectonophysics 302, 23–40.

Claypool, G.E., Holser, W.T., Kaplan, I.R., Sakai, H., Zak, I., 1980. The age curves of sulfur and oxygen isotopes in marine sulfate and their mutual interpretation. Chem. Geol. 28, 199–260.

Dare, S.A.S., Barnes, S.J., Beaudoin, G., 2012. Variation in trace element content of magnetite crystallized from a fractionating sulfide liquid, Sudbury, Canada: implications for provenance discrimination. Geochim. Cosmochim. Acta 88, 27–50.

Dill, H.G., 2010. The "chessboard" classification scheme of mineral deposits: mineralogy and geology from aluminum to zirconium. Earth Sci. Rev. 100, 1–420.

Ding, T.P., Vaikiers, S., Wan, D.F., Bai, R.M., Zou, X.Q., Li, Y.H., Zhang, Q.L., Bievre, P.D., 2001. The $\delta^{33}S$ and $\delta^{34}S$ values and absolute $^{32}S/^{33}S$ and $^{32}S/^{34}S$ ratios of IAEA and Chinese sulfur isotope reference materials. Bull. Mineral. Petrol. Geochem. 20, 425–427 (in Chinese with English abstract).

Dong, F.R., Li, S.L., Feng, X.C., 1996. Low-pressure granulite facies in Weiya area of East Tian Shan, Xinjiang. Xinjiang Geol. 14, 151–158 (in Chinese with English abstract).

Dupuis, C., Beaudoin, G., 2011. Discriminant diagrams for iron oxide trace element fingerprinting of mineral deposit types. Mineral. Deposita 46, 1–17.

Fang, G.Q., 1994. Paleozoic plate tectonics of Eastern Tianshan mountains Xinjiang, China. Acta Geol. Gansu 3, 34–40 (in Chinese with English abstract).

Gao, Z.J., Chen, J.X., Lu, S.N., 1993. Precambrian Geology of Northern Xinjiang. Geological Publishing House, Beijing, pp. 1–171, (in Chinese).

Gao, J.F., Zhou, M.F., LightFoot, P.C., Wang, C.Y., Qi, L., Sun, M., 2013. Sulfide saturation and magma emplacement in the formation of the Permian Huangshandong Ni–Cu sulfide deposit, Xinjiang, Northwestern China. Econ. Geol. 108, 1833–1848.

Goldhaber, M.B., Kaplan, I.R., 1982. Controls and consequences of sulfate reduction rates in recent marine sediments. Acid Sulfate Weathering 119, 19–36.

Hou, T., Zhang, Z., Pirajno, F., Santosh, M., Encarnacion, J., Liu, J., Zhao, Z., Zhang, L., 2014a. Geology, tectonic settings and iron ore metallogenesis associated with submarine volcanism in China: an overview. Ore Geol. Rev. 57, 498–517.

Hou, T., Zhang, Z., Santosh, M., Encarnacion, J., Zhu, J., Luo, W., 2014b. Geochronology and geochemistry of submarine volcanic rocks in the Yamansu iron deposit, Eastern Tianshan Mountains, NW China: constraints on the metallogenesis. Ore Geol. Rev. 56, 487–502.

Hu, A.Q., Zhang, J.B., Zhang, Z.G., Zhao, D.J., Liu, J.Y., Yang, S.Z., Peng, J.H., Zhou, W., 1986. U–Pb age and evolution of Precambrian metamorphic rocks of middie Tianshan uplift zone, eastern Tianshan, China. Geochimica 23–25 (in Chinese with English abstract).

Hu, A., Zhang, G., Zhang, Q., Chen, Y., 1998. Constraints on the age of basement and crustal growth in Tianshan Orogen by Nd isotopic composition. Sci. China Ser. D 41, 648–657.

Hu, A., Jahn, B.-m., Zhang, G., Chen, Y., Zhang, Q., 2000. Crustal evolution and Phanerozoic crustal growth in northern Xinjiang: Nd isotopic evidence. Part I. Isotopic characterization of basement rocks. Tectonophysics 328, 15–51.

Hu, A.Q., Wei, G.J., Zhang, J.B., Deng, W.F., Chen, L.L., 2007. SHRIMP U–Pb age for zircons of East Tianhu granitic gneiss and tectonic evolution significance from the eastern Tianshan Mountains, Xinjiang, China. Acta Petrol. Sin. 23, 1795–1802 (in Chinese with English abstract).

Huang, X.W., Qi, L., Gao, J.F., Zhou, M.F., 2013a. First reliable Re–Os ages of pyrite and stable isotope compositions of Fe(–Cu) deposits in the Hami region, Eastern Tianshan Orogenic Belt, NW China. Resour. Geol. 63, 166–187.

Huang, X.W., Zhao, X.F., Qi, L., Zhou, M.F., 2013b. Re–Os and S isotopic constraints on the origins of two mineralization events at the Tangdan sedimentary rock-hosted stratiform Cu deposit, SW China. Chem. Geol. 347, 9–19.

Huang, X.W., Zhou, M.F., Qi, L., Gao, J.F., Wang, Y.W., 2013c. Re–Os isotopic ages of pyrite and chemical composition of magnetite from the Cihai magmatic–hydrothermal Fe deposit, NW China. Mineral. Deposita 48, 925–946.

Huang, X.W., Qi, L., Wang, Y.C., Liu, Y.Y., 2014. Re–Os dating of magnetite from the Shaquanzi Fe–Cu deposit, eastern Tianshan, NW China. Sci. China Earth Sci. 57, 267–277.

IGCAS (Institute of Geochemistry, Chinese Academy of Sciences), 1976. Preliminary sulfur isotopic composition of sulfides from the Tianhu Fe deposit, unpublished Geology report, (in Chinese).

Jahn, B., Wu, F., Chen, B., 2000. Granitoids of the Central Asian Orogenic Belt and continental growth in the Phanerozoic. Trans. R. Soc. Edinb. Earth Sci. 91, 181–194.

Jahn, B., Windley, B., Natal'in, B., Dobretsov, N., 2004. Phanerozoic continental growth in Central Asia. J. Asian Earth Sci. 23, 599–603.

Ji, J.S., Tao, H.X., Zeng, Z.R., Yang, X.K., Zhang, L.C., 1994. Geology and Mineralization of the Kangurtag Gold Belt in Eastern Tianshan. Geological Publishing House, Beijing, pp. 1–20, (in Chinese).

Jia, Q.Z., 1991. A discussion on the ore genesis of Tianhu iron deposit: constrains from the typomorphic features of magnetite. NW Geol. 12, 19–25 (in Chinese).

Kirk, J., Ruiz, J., Chesley, J., Titley, S., Walshe, J., 2001. A detrital model for the origin of gold and sulfides in the Witwatersrand basin based on Re–Os isotopes. Geochim. Cosmochim. Acta 65, 2149–2159.

Kiyosu, Y., 1980. Chemical reduction and sulfur-isotope effects of sulfate by organic matter under hydrothermal conditions. Chem. Geol. 30, 47–56.

Lambert, D.D., Foster, J.G., Frick, L.R., Hoatson, D.M., Purvis, A.C., 1998. Application of the Re–Os isotopic system to the study of Precambrian magmatic sulfide deposits of Western Australia. Aust. J. Earth Sci. 45, 265–284.

Lei, R.-X., Wu, C.-Z., Gu, L.-X., Zhang, Z.-Z., Chi, G.-X., Jiang, Y.-H., 2011. Zircon U–Pb chronology and Hf isotope of the Xingxingxia granodiorite from the Central Tianshan zone (NW China): Implications for the tectonic evolution of the southern Altaids. Gondwana Res. 20, 582–593.

Li, H.Q., Chen, F.W., 2003. Isotopic Geochronology of Regional Mineralization in Xinjiang, NW China. Geological Publishing House, Beijing, (in Chinese).

Li, W.P., Wang, T., Li, J.B., Kang, X., Yu, F.S., Han, Q.J., Ma, Z.P., 2001. The U–Pb age of zircon from Late Caledonian granitoids in Hongliuhe area, East Tianshan mountains, Northwest China and its geological implications. Acta Geolsci. Sin. 22, 231–235 (in Chinese with English abstract).

Li, Q., Liu, S., Han, B., Zhang, J., Chu, Z., 2005. Geochemistry of metasedimentary rocks of the Proterozoic Xingxingxia Complex: implications for provenance and tectonic setting of the Eastern Segment of the Central Tianshan Tectonic Zone, Northwestern China. Can. J. Earth Sci. 42, 287–306.

Liu, S., Guo, Z., Zhang, Z., Li, Q., Zheng, H., 2004. Nature of the Precambrian metamorphic blocks in the eastern segment of Central Tianshan: constraint from geochronology and Nd isotopic geochemistry. Sci. China Ser. D Earth Sci. 47, 1085–1094.

Liu, Y., Hu, Z., Gao, S., Günther, D., Xu, J., Gao, C., Chen, H., 2008. *In situ* analysis of major and trace elements of anhydrous minerals by LA-ICP-MS without applying an internal standard. Chem. Geol. 257, 34–43.

Loftus-Hills, G., Solomon, M., 1967. Cobalt, nickel and selenium in sulphides as indicators of ore genesis. Mineral. Deposita 2, 228–242.

Ludwig, K.R., 1980. Calculation of uncertainties of U–Pb isotope data. Earth Planet. Sci. Lett. 46, 212–220.

Ludwig, K.R., 2003. A geochronological toolkit for Microsoft Excel. Berkeley Geochronology Center Special Publication No. 4,pp. 1–70.

Luo, G.Y., Zhu, J.R., 1986. The Precambrian metamorphic minerlization in China. Symposium of International Proceedings in Precambrian Crustal Evolution Series Two: Geochemistry and Mineralization of Metamorphic Rock. Geological Publishing House, Beijing, pp. 172–188 (in Chinese with English abstract).

Ma, R.S., Wang, C.Y., Ye, S.F., 1993. Tectonic Framework and Crust Evolution of Eastern Tianshan. Nanjing University Press, Nanjing, pp. 1–202, (in Chinese).

Ma, R.S., Shu, L.S., Sun, J.Q., 1997. Tectonic Evolution and Mineralization of Eastern Tianshan. Geological Publishing House, Beijing, (in Chinese).

Ma, X., Shu, L., Santosh, M., Li, J., 2012. Detrital zircon U–Pb geochronology and Hf isotope data from Central Tianshan suggesting a link with the Tarim Block: implications on Proterozoic supercontinent history. Precambrian Res. 206, 1–16.

Ma, X., Shu, L., Santosh, M., Li, J., 2013. Paleoproterozoic collisional orogeny in Central Tianshan: assembling the Tarim Block within the Columbia supercontinent. Precambrian Res. 228, 1–19.

Mao, J.W., Goldfarb, R.J., Wang, Y.T., Hart, C.J., Wang, Z.L., Yang, J.M., 2005. Late Paleozoic base and precious metal deposits, East Tianshan, Xinjiang, China: characteristics and geodynamic setting. Episodes 28, 23–30.

Mathur, R., Ruiz, J., Munizaga, F., 2000. Relationship between copper tonnage of Chilean base-metal porphyry deposits and Os isotope ratios. Geology 28, 555–558.

Mathur, R., Marschik, R., Ruiz, J., Munizaga, F., Leveille, R.A., Martin, W., 2002. Age of mineralization of the Candelaria Fe oxide Cu–Au deposit and the origin of the Chilean iron belt, based on Re–Os isotopes. Econ. Geol. 97, 59–71.

Mathur, R., Gauert, C., Ruiz, J., Linton, P., 2012. Evidence for mixing of Re–Os isotopes at <2.7 Ga and support of a remobilized placer model in Witwatersrand sulfides and native Au. Lithos 164–167, 65–73.

Morelli, R.M., Creaser, R.A., Selby, D., Kelley, K.D., Leach, D.L., King, A.R., 2004. Re–Os sulfide geochronology of the red dog sediment-hosted Zn–Pb–Ag deposit, Brooks Range, Alaska. Econ. Geol. 99, 1569–1576.

Morgan, J.W., Stein, H.J., Hannah, J.L., Markey, R.J., Wiszniewska, J., 2000. Re–Os study of Fe–Ti–V oxide and Fe–Cu–Ni sulfide deposits, Suwalki Anorthosite Massif, northeast Poland. Mineral. Deposita 35, 391–401.

Müller, B., Axelsson, M.D., Öhlander, B., 2003. Trace elements in magnetite from Kiruna, northern Sweden, as determined by LA-ICP-MS. GFF 125, 1–5.
Nadoll, P., Mauk, J.L., Hayes, T.S., Koenig, A.E., Box, S.E., 2012. Geochemistry of magnetite from hydrothermal ore deposits and host rocks of the Mesoproterozoic Belt Supergroup, United States. Econ. Geol. 107, 1275–1292.
Nadoll, P., Angerer, T., Mauk, J.L., French, D., Walshe, J., 2014. The chemistry of hydrothermal magnetite: a review. Ore Geol. Rev. 61, 1–32.
Orr, W.L., 1974. Changes in sulfur content and isotopic ratios of sulfur during petroleum maturation; study of big horn basin Paleozoic oils. AAPG Bull. 58, 2295–2318.
Pirajno, F., Mao, J.W., Zhang, Z.C., Zhang, Z.H., Chai, F.M., 2008. The association of mafic–ultramafic intrusions and A-type magmatism in the Tian Shan and Altay orogens, NW China: implications for geodynamic evolution and potential for the discovery of new ore deposits. J. Asian Earth Sci. 32, 165–183.
Qi, L., Hu, J., Gregoire, D.C., 2000. Determination of trace elements in granites by inductively coupled plasma mass spectrometry. Talanta 51, 507–513.
Qi, L., Zhou, M.-F., Wang, C.Y., Sun, M., 2007. Evaluation of a technique for determining Re and PGEs in geological samples by ICP-MS coupled with a modified Carius tube digestion. Geochem. J. 41, 407–414.
Qi, L., Zhou, M.-F., Gao, J., Zhao, Z., 2010. An improved Carius tube technique for determination of low concentrations of Re and Os in pyrites. J. Anal. At. Spectrom. 25, 585–589.
Qin, K.Z., Fang, T.H., Wang, S.L., Zhu, B.Q., Feng, Y.M., Yu, H.F., Xiu, Q.Y., 2002. Plate tectonics division, evolution and metallogenic settings in eastern Tianshan Mountains, NW China. Xinjiang Geol. 20, 302–308 (in Chinese with English abstract).
Rudnick, R.L., Gao, S., 2003. Composition of the continental crust. In: Holland, H.D., Turekian, K.K. (Eds.), Treatise on Geochemistry. Elsevier-Pergaman, Oxford, pp. 1–64.
Ruiz, J., Mathur, R., 1999. Metallogenesis in continental margins: Re–Os evidence from porphyry copper deposits in Chile. In: Lambert, D.D., Ruiz, J. (Eds.), Application of Radiogenic Isotopes to Ore Deposit Research and Exploration. Rev. Econ. Geol. pp. 59–72
Rusk, B.G., Oliver, N., Brown, A., Lilly, R., Jungmann, D., 2009. Barren magnetite breccias in the Cloncurry region, Australia; comparisons to IOCG deposits. Smart Science for Exploration and Mining, Proceedings of the 10th Biennial Society for Geology Applied to Mineral Deposits (SGA) Meeting. Townsville, pp. 656–658.
Schoenberg, R., Nägler, T.F., Kramers, J.D., 2000. Precise Os isotope ratio and Re–Os isotope dilution measurements down to the picogram level using multicollector inductively coupled plasma mass spectrometry. Int. J. Mass Spectrom. 197, 85–94.
Selby, D., Kelley, K.D., Hitzman, M.W., Zieg, J., 2009. Re–Os sulfide (bornite, chalcopyrite, and pyrite) systematics of the carbonate-hosted copper deposits at Ruby Creek, southern Brooks range, Alaska. Econ. Geol. 104, 437–444.
Sengör, A.M.C., Burtman, V.S., 1993. Evolution of the Altaid tectonic collage and Palaeozoic crustal growth in Eurasia. Nature 364, 299–307.
Shirey, S.B., Walker, R.J., 1995. Carius tube digestion for low-blank rhenium–osmium analysis. Anal. Chem. 67, 2136–2141.
Shu, L.S., Charvet, J., Lu, H.F., Laurent-Charvet, S., 2002. Paleozoic accretion–collision events and kinematics of deformation in the eastern part of the Southern-Central Tianshan belt, China. Acta Geol. Sin. 76, 308–323.
Singoyi, B., Danyushevsky, L., Davidson, G.J., Large, R., Zaw, K., 2006. Determination of trace elements in magnetites from hydrothermal deposits using the LA ICP-MS technique. SEG Keystone Conference. CD-ROM, Denver, USA.
Song, Z.G., Lou, C.Y., Shi, Z.Y., Li, J.X., Jia, Q.Z., Meng, F.Y., 1989. A discussion on characteristics, type and origin of Tianhu iron ore deposit in Xinjiang. Bu. Xi'an Inst. Geol. Mineral Resour. Chin. Acad. Geol. Sci. 26, 43–58 (in Chinese with English abstract).
Spry, P.G., Mathur, R.D., Bonsall, T.A., Voudouris, P.C., Melfos, V., 2013. Re–Os isotope evidence for mixed source components in carbonate-replacement Pb–Zn–Ag deposits in the Lavrion district, Attica, Greece. Mineral. Petrol. http://dx.doi.org/10.1007/s00710-013-0314-2.
Stein, H.J., Morgan, J.W., Schersten, A., 2000. Re–Os dating of Low-Level Highly Radiogenic (LLHR) sulfides: the Harnäs gold deposit, southwest Sweden, records continental-scale tectonic events. Econ. Geol. 95, 1657–1671.
Tristá-Aguilera, D., Barra, F., Ruiz, J., Morata, D., Talavera-Mendoza, O., Kojima, S., Ferraris, F., 2006. Re–Os isotope systematics for the Lince–Estefanía deposit: constraints on the timing and source of copper mineralization in a stratabound copper deposit, Coastal Cordillera of Northern Chile. Mineral. Deposita 41, 99–105.
Velasco, F., Sánchez-España, J., Boyce, A.J., Fallick, A.E., Sáez, R., Almodóvar, G.R., 1998. A new sulphur isotopic study of some Iberian Pyrite Belt deposits: evidence of a textural control on sulphur isotope composition. Mineral. Deposita 34, 4–18.
Wang, Y.W., Wang, J.B., Wang, L.J., Qin, Q.X., Peng, X.M., Hui, W.D., 2005. Weiya vanadium-bearing titanomagnetite deposit in Xinjiang: a polygenetic magmatic differentiation–magmatic injection–magmatic hydrothermal deposit. Mineral. Deposita 24, 349–360 (in Chinese with English abstract).
Wang, D.H., Li, C.J., Chen, Z.H., Chen, S.P., Xiao, K.Y., Li, H.Q., Liang, T., 2006. Metallogenic characteristics and direction in mineral research in east Tianshan, Xinjiang, China. Geol. Bull. Chin. 25, 910–915 (in Chinese with English abstract).
Windley, B.F., Alexeiev, D., Xiao, W., Kröner, A., Badarch, G., 2007. Tectonic models for accretion of the Central Asian Orogenic Belt. J. Geol. Soc. 164, 31–47.
Xia, L.Q., Xia, Z.C., Xu, X.Y., Li, X.M., Ma, Z.P., 2008. Relative contributions of crust and mantle to the generation of the Tianshan Carboniferous rift-related basic lavas, northwestern China. J. Asian Earth Sci. 31, 357–378.
Xiao, W.J., Zhang, L.C., Qin, K.Z., Sun, S., Li, J.L., 2004. Paleozoic accretionary and collisional tectonics of the Eastern Tianshan (China): implications for the continental growth of central Asia. Am. J. Sci. 304, 370–395.
Xiao, W., Han, C., Yuan, C., Sun, M., Lin, S., Chen, H., Li, Z., Li, J., Sun, S., 2008. Middle Cambrian to Permian subduction-related accretionary orogenesis of Northern Xinjiang, NW China: implications for the tectonic evolution of central Asia. J. Asian Earth Sci. 32, 102–117.
Xiao, W.J., Windley, B.F., Huang, B.C., Han, C.M., Yuan, C., Chen, H.L., Sun, M., Sun, S., Li, J.L., 2009a. End-Permian to mid-Triassic termination of the accretionary processes of the southern Altaids: implications for the geodynamic evolution, Phanerozoic continental growth, and metallogeny of Central Asia. Int. J. Earth Sci. 98, 1189–1217.
Xiao, W.J., Windley, B.F., Yuan, C., Sun, M., Han, C.M., Lin, S.F., Chen, H.L., Yan, Q.R., Liu, D.Y., Qin, K.Z., 2009b. Paleozoic multiple subduction–accretion processes of the southern Altaids. Am. J. Sci. 309, 221–270.
Xiong, Y., Wood, S.A., 1999. Experimental determination of the solubility of ReO_2 and the dominant oxidation state of rhenium in hydrothermal solutions. Chem. Geol. 158, 245–256.
Xiong, Y., Wood, S., Kruszewski, J., 2006. Hydrothermal transport and deposition of rhenium under subcritical conditions revisited. Econ. Geol. 101, 471–478.
Xiu, Q.Y., Yu, H.F., Li, Q., 2002. A single zircon U–Pb age for the granodiorite of Kawabulak complex, Xinjiang, China. Xinjiang Geol. 20, 335–337 (in Chinese with English abstract).
Yang, X.K., Ji, J.S., Luo, G.C., Tao, H.X., 1997. Plate tectonics and forming law of the metallic ore deposits in eastern Tianshan. J. Xi'an Coll. Geol. 19, 34–42 (in Chinese with English abstract).
Yao, P.H., Wang, K.N., Dun, C.L., Lin, Z.T., Song, X., 1993. Records of China's Iron Ore Deposits. Metallurgical Industry Press, Beijing, (in Chinese with English abstract).
Zhang, G.Y., 1985. On the mechanism of alkali-metasomatism in the main types of endogenic iron deposit in China. Geochimica 58–66 (in Chinese with English abstract).
Zhang, C.W., 1994. Plate tectonics and its evolution of Eastern Xinjiang and adjacent areas. J. Chengdu Inst. Tech. 21, 1–10 (in Chinese with English abstract).
Zhang, Z.Z., Gu, L.X., Wu, C.Z., Li, W.Q., Xi, A.H., Wang, S., 2005. Zircon SHRIMP dating for the Weiya pluton, eastern Tianshan: its geological implications. Acta Geol. Sin. 79, 481–490 (in Chinese with English abstract).
Zhang, Z., Zhou, G., Kusky, T.M., Yan, S., Chen, B., Zhao, L., 2009. Late Paleozoic volcanic record of the Eastern Junggar terrane, Xinjiang, Northwestern China: major and trace element characteristics, Sr–Nd isotopic systematics and implications for tectonic evolution. Gondwana Res. 16, 201–215.
Zhang, Z., Hou, T., Santosh, M., Li, H., Li, J., Zhang, Z., Song, X., Wang, M., 2014. Spatio-temporal distribution and tectonic settings of the major iron deposits in China: an overview. Ore Geol. Rev. 57, 247–263.
Zhao, B., 1989. Skarn deposits formed by migmatization. Main Skarns and Skarn Deposits in China. Science Press, Beijing, pp. 254–257 (Ed., in Chinese with English abstract).
Zhou, D., Graham, S.A., Chang, E.Z., Wang, B., Bradley, H., 2001. Paleozoic amalgamation of the Chinese Tian Shan: evidence from a transect along the Dushanzi–Kuqa Highway. In: Hendrix, M.S., Davis, G.A. (Eds.), Paleozoic and Mesozoic Tectonic Evolution of Central and Eastern Asia: From Continental Assembly to Intracontinental Deformation. Geol. Soc. Am. Mem. 194, pp. 23–46.